International Journal for Numerical Methods in Engineering

WILEY

RESEARCH ARTICLE OPEN ACCESS

On the Influence of the Fiber Curvature on the Stiffness of Long Fiber Reinforced Composites

Celine Lauff[1] | Maximilian Krause[2] | Matti Schneider[2] | Thomas Böhlke[1]

[1]Institute of Engineering Mechanics, Karlsruhe Institute of Technology (KIT), Karlsruhe, Germany | [2]Institute of Engineering Mathematics, University of Duisburg-Essen, Essen, Germany

Correspondence: Celine Lauff (celine.lauff@kit.edu)

Received: 11 March 2025 | **Revised:** 5 June 2025 | **Accepted:** 16 July 2025

Funding: This work was supported by the Deutsche Forschungsgemeinschaft (Grant No. 255730231) and the HORIZON EUROPE European Research Council (Grant No. 101040238).

Keywords: curvature control | curved fibers | fused sequential addition and migration | long fiber reinforced composites | microstructure generation | representative volume elements

ABSTRACT

The degree of curvature of fiber inclusions in fiber-reinforced composites impacts the elastic properties of the composite, but numerical studies of this effect are limited by the lack of efficient microstructure generators with fiber curvature control. We propose an extension to the fused Sequential Addition and Migration algorithm (*Int. J. Numer. Methods Eng.*, 125(22), e7573, 2024) to allow for the direct control of the average fiber curvature. To this end, we prescribe an averaged curvature parameter for the entire microstructure, while also constraining local curvature for every fiber to a maximum value. While local curvature is unambiguously defined, the choice of the averaged curvature parameter is not obvious. We introduce as a novel curvature measure the deviation from straight curve (DSC), which computes as the trace of the local second-order fiber orientation tensor's covariance for a single fiber. Averaging this over all fibers leads to a scalar averaged curvature parameter. Using this parameter, we define an optimization procedure for generating curved-fiber reinforced microstructures. We compare the microstructure generation capabilities of the proposed extension with the prior algorithm without curvature control and find that the extended algorithm is capable of realizing a significantly wider spectrum of curvatures. Finally, we study the influence of fiber curvature on elastic properties, and find that for an example composite of glass-fiber reinforced polypropylene, increased fiber curvature leads to a reduction of the Young's modulus by as much as 10%.

1 | Introduction

1.1 | State of the Art

Discontinuous fiber-reinforced composites are central for lightweight technologies due to their high specific stiffness, design freedom, and mass-production capabilities [1–3]. Micro-CT imaging [4–8] reveals that the microstructure is heterogeneous, random, and anisotropic. To leverage discontinuous fiber-reinforced composites for lightweight applications, tools are needed to predict their mechanical properties while accounting for the characteristics of the microstructure. To do so, experimental characterization of the mechanical properties may be used. However, experiments are generally resource- and time-intensive, and do not cover the entire range of possible fiber arrangements. Thus, computational multiscale methods [9–11]

based on homogenization theory [12, 13] complement the experiments, requiring a representative geometrical description of the microstructure.

Typically, such geometries are obtained from micro-CT imaging or from synthetic microstructure generation. Whereas real image data comes with a high expense for a single realization, microstructure generation is an efficient approach to reconstruct geometries for a wide span of descriptors, for example, the fiber volume fraction or the fiber length distribution. To decrease the boundary artifacts and the necessary cell size for representativity, periodic geometries are advantageous [14–16]. However, geometries extracted from real image data are non-periodic, and a subsequent periodization is non-trivial. In contrast, simple strategies may be applied to account for the periodicity as part of microstructure generation tools. These advantages motivate the development of efficient microstructure generation tools to obtain representative geometries with periodic descriptions [17, 18].

Microstructure generation tools for particle-reinforced composites are classically divided into two groups with respect to the packing procedure. The sequential insertion algorithms arrange the particles consecutively within the unit cell, and the location of an inserted particle is fixed. In this category, the random sequential addition (RSA) [19, 20] is the most commonly used representative. Particle by particle, the unit cell is filled up to the desired volume fraction under the condition that no overlap is detected. For the special case of short fibers, each fiber is modeled as a cylinder, and the fiber lengths, the fiber directions, and the fiber midpoints are sampled from prescribed distribution functions. Due to its prominence, many extensions of the RSA algorithm are available [21–25]. Whereas the RSA algorithm is capable of packing microstructures up to high fiber volume fractions for the unidirectional orientation state, the fiber volume fraction is limited when considering more general fiber-orientation states and moderate to high fiber-aspect ratios, that is, the ratios between lengths and diameters. For almost planar fiber arrangements, the sequential deposition algorithm [26, 27] permits the generation of high fiber volume fractions, even for large fiber aspect ratios. The algorithm simulates fibers dropping into the unit cell under the influence of gravity and is capable of accounting for the flexibility of the fibers.

The second category of microstructure generators comprises collective rearrangement algorithms. These move all the particles at the same time, which is closer to typical manufacturing processes and enables more flexibility to reach high fiber volume fractions. For instance, the mechanical contraction method (MCM) [28] models the fibers as spherocylinders, that is, cylinders with half-caps at their ends, and first generates a packing with low fiber volume fraction using the RSA. In a second step, the dimensions of the cell, but not the fibers, are decreased. To resolve the resulting overlaps, fibers are displaced and rotated in a clever fashion. Whereas the MCM generates isotropic orientation states, the sequential addition and migration (SAM) algorithm [29] for short fibers with uniform length is applicable to general orientation distributions. As the starting configuration, fibers are sampled up to the desired fiber volume fraction, accounting for the prescribed fiber orientation distribution. In contrast to the MCM, the starting configuration includes fiber overlap. Subsequently, an optimization procedure is used to find a non-overlapping fiber configuration that fulfills additional criteria, for example, the desired fiber orientation state. Further publications extend the SAM algorithm to realize fiber length distributions [30] and to account for coupled fiber length and orientation distributions [31]. For the SAM algorithm with straight fibers, the required edge length of the unit cell increases linearly with the fiber length, and the cells are quite large for long fibers. As the computational effort for the microstructure generation and the computational homogenization is elevated for larger cell sizes, such an algorithmic characteristic is extremely limiting. Another shortcoming when applying the SAM algorithm to long fibers concerns the arrangement of the fibers in almost aligned bundle structures, which is not representative of real microstructures and may lead to distortions in the predicted mechanical behavior. Last but not least, the SAM algorithm with straight fibers does not account for bent fibers, even though the fiber curvature may affect the mechanical behavior [32–35]. This effect is particularly relevant for long fiber reinforced microstructures.

Fliegener et al. [36] as well as Abd El-Rahman and Tucker [37] present approaches which are applicable to high fiber volume fractions, large fiber aspect ratios, and account for the fiber bending. Starting with a fiber configuration with low fiber volume fraction generated by the RSA algorithm, a full finite element analysis is used to compress the microstructure in the out-of-plane direction until the desired fiber volume fraction is reached. Due to the compression in the thickness direction, the orientation states are mainly planar, which is typical for discontinuous fiber-reinforced composites [1, 38–40]. However, the computational expense to obtain a single realization is quite high as a result of the full finite element approach, including a fine resolution of the fibers.

The SAM algorithm for long fibers [33] represents a more efficient optimization-based approach, modeling the fibers as polygonal chains with cylindrical segments. Due to this modeling approach, the objective function incorporates an additional term to ensure the connectivity of adjacent segments. Unfortunately, the extension has the adverse effect that the realizable fiber volume fraction is significantly lower than for the original formulation. As an alternative strategy, the fused sequential addition and migration (fSAM) method [41] does not interpret the connectivity constraint as a condition which is only required for convergence but as a condition which is mandatory for each iteration step. Thus, the optimization is restricted to the curved, that is, non-flat, configuration space of a connected fiber. As the iterates of a basic gradient descent approach may leave the curved optimization space, an adapted iteration rule is used. To do so, the iterates are computed by moving along the geodesics, that is, the shortest path between two points on the curved optimization space. Such a procedure replaces the additional term in the objective function as it ensures that each iterate is admissible in terms of the connectivity constraint. As a result of its optimization-based approach with an adapted iteration rule, the fSAM algorithm features an improved convergence behavior, which enables the application to complex microstructures with, for example, high fiber volume fractions and large fiber aspect ratios. Additionally, an extension of the fSAM algorithm [42] enables the generation of microstructures for hybrid fiber-reinforced composites—for

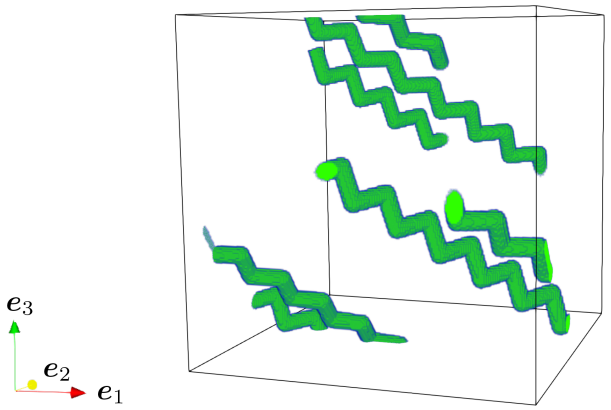

FIGURE 1 | Single fiber with a high mean of the local curvature.

example, continuous-discontinuous fiber-reinforced composites [43]—or to account for areas with varying characteristics within the microstructure, for example, the skin-core-skin structure of discontinuous fiber-reinforced composites [44–46].

1.2 | Contributions

This work investigates the influence of different degrees of average fiber curvature on the elastic properties of fiber-reinforced microstructures. To generate microstructures with a specific curvature, a quantitative curvature parameter needs to be defined. The mean of the local curvature, which would be a straightforward choice, is unsuitable. High local curvature values can be realized by frequently alternating changes of fiber direction along the fiber length. Thus, the mean of the local curvature can be increased without changing the overall shape of the fiber, as shown in Figure 1. However, for real fibers, we typically observe smooth transitions in the fiber directions and significant changes in the overall shape. Thus, the fiber zig-zagging shown in Figure 1 is not representative of physical fiber bending. To avoid this pathological behavior, we introduce the deviation from straight curve (DSC) as a novel curvature measure for fiber composites, which computes as the trace of the local second-order fiber orientation tensor's covariance for a single fiber, and show that constraints on this parameter serve as constraints on the mean of the local curvature. To avoid excessively high local curvature values, which would lead to real fibers breaking, we also restrict the local curvature to a critical threshold. With the condition of the local curvature constraint, prescribing the DSC leads to fibers with physically meaningful fiber bending, especially without zig-zagging or sharp bends.

In Section 3, we implement the global curvature objective and local curvature constraint into the fused Sequential Addition and Migration (fSAM) [41] algorithm for generating curved fiber microstructures. The fSAM algorithm is already capable of generating periodic microstructures containing curved fibers; however, the average curvature of the fibers cannot be controlled directly and results indirectly from other parameters such as fiber volume fraction and length distribution. As the fSAM algorithm discretizes fibers as chains of straight segments, the local curvature cannot be computed exactly, and we find a suitable approximation. Implementing the curvature objective and constraint amounts to adding two additional terms to the objective function. To minimize this novel objective function, we adapt the optimization procedure from the non-curvature-controlled version of the fSAM algorithm, requiring minimal changes.

Section 4 contains computational studies of the curvature-controlled fSAM algorithm for glass-fiber reinforced polypropylene. For realistic example values of the fiber aspect ratio and volume fraction, we investigate the realizable limits of curvature. At both high and low curvature values, we quantify the error due to RVE size and voxel resolution. We also discuss the effect of the segment length, which is a numerical parameter arising from the discretization of the fibers as chains of straight segments. Using the results from the numerical parameter studies, we finally quantify the influence of fiber curvature on the mechanical properties of the glass-fiber reinforced polypropylene.

1.3 | Notation

In this manuscript, we employ direct tensor notation or matrix-vector notation with orthonormal bases $\{\boldsymbol{e}_1, \ldots, \boldsymbol{e}_n\}$ with $n \in \mathbb{N}$. Scalars are represented by non-bold letters, for example, b. For the matrix-vector notation, we denote vectors with non-cursive bold lowercase letters, for example, $\mathbf{b}$, while bold non-cursive uppercase letters, for example, $\mathbf{B}$, represent matrices. For the direct tensor notation, we use cursive bold lowercase letters (e.g., $\boldsymbol{b}$) for vectors, bold cursive uppercase letters (e.g., $\boldsymbol{B}$) for second-order tensors, and blackboard bold uppercase letters (e.g., $\mathbb{B}$) for fourth-order tensors. A symmetric tensor of second order defined in a three-dimensional vector space is represented with, for example, $\boldsymbol{B} \hat{=} \operatorname{diag}(b_1, b_2, b_3)$, in its diagonalized form. The identity tensor of second order denotes $\boldsymbol{I} \hat{=} (\boldsymbol{I})_{ij} = \delta_{ij}$ with the Kronecker delta δ_{ij}, and we denote the identity matrix with $\mathbf{1}_{n\times n}$, where n is the dimension. We introduce the notation of the mathematical operations with respect to the direct tensor notation, but use the same notation for the operations in matrix-vector notation as well. The transposed tensor of second order reads, for example, $\boldsymbol{B}^{\mathrm{T}}$, and the linear mapping of a tensor of first order by a tensor of second order is represented by, for example, $\boldsymbol{a} = \boldsymbol{C}\boldsymbol{b}$. The linear mappings with complete contraction, including higher-order tensors, are expressed as, for example, $\boldsymbol{a} = \mathbb{B}\left[\boldsymbol{C}_{\langle 3\rangle}\right] \hat{=} B_{ijkl}C_{jkl}$. For the trace of a second-order tensor, we use, for example, $\operatorname{tr}(\boldsymbol{B}) = B_{ii}$, and for a fourth-order tensor, we define the trace operator, for example, $\operatorname{tr}(\mathbb{B}) = B_{ijij}$. The scalar product is indicated by, for example, $\boldsymbol{A} \cdot \boldsymbol{B} = \operatorname{tr}\left(\boldsymbol{A}\boldsymbol{B}^{\mathrm{T}}\right)$ and the Frobenius norm is symbolized by, for example, $\|\boldsymbol{B}\| = (\boldsymbol{B} \cdot \boldsymbol{B})^{1/2}$. For the dyadic product, we use, for example, $\boldsymbol{a} \otimes \boldsymbol{b}$ and abbreviate the l-times repeated dyadic product with, for example, $\boldsymbol{b}^{\otimes l} = \boldsymbol{b} \otimes \boldsymbol{b} \cdots \otimes \boldsymbol{b}$. The expression S^2 denotes the unit sphere in $\mathbb{R}^3$. The cross product of two vectors is expressed with, for example, $\boldsymbol{a} \times \boldsymbol{b}$, and we denote a skew-symmetric tensor of second order with corresponding axial vector $\boldsymbol{b}$ by $\boldsymbol{b}\times \hat{=} (\boldsymbol{b}\times)_{ij} = \epsilon_{ikj}b_k$, where $\boldsymbol{\epsilon}$ is the permutation symbol.

2 | Description and Discretization of Curved Fibers

2.1 | Quantifying the Orientation and the Curvature of a Single Fiber

We consider a fiber with length L and constant diameter D whose centerline may be described by a twice continuously differentiable curve

$$\boldsymbol{c} : [0, L] \to Q \tag{2.1}$$

within the periodic unit cell $Q = [0, Q_1] \times [0, Q_2] \times [0, Q_3]$. Such a representation is illustrated in Figure 2.

We assume that the curve $\boldsymbol{c}$ is parametrized by arc length s, that is, the first derivative of the curve has unit length

$$\|\boldsymbol{c}'(s)\| = 1, \quad s \in [0, L] \tag{2.2}$$

According to Pappus' theorem [47], the fiber volume fraction of a fiber with circular cross-section equals the fiber volume fraction of a straight cylinder, regardless of the curved shape of the fiber, that is, the expression

$$\phi_f = \frac{\pi L D^2}{4 Q_1 Q_2 Q_3} \tag{2.3}$$

is valid. As a consequence, in case all fibers have equal diameter, the fiber-volume fraction of a collection of non-overlapping fibers is solely determined by the total fiber length.

The statistics of the fiber orientation state of fiber ensembles is compactly described by the fiber orientation tensors of second order $\boldsymbol{A}_f$ and of fourth order $\mathbb{A}_f$ [48, 49]. For a single fiber, these tensors take the form

$$\boldsymbol{A}_f = \frac{1}{L}\int_0^L \boldsymbol{c}'(s) \otimes \boldsymbol{c}'(s)\, ds \quad \text{and} \quad \mathbb{A}_f = \frac{1}{L}\int_0^L \left(\boldsymbol{c}'(s)\right)^{\otimes 4}\, ds \tag{2.4}$$

Due to the normalization condition (2.2) satisfied by the vector $\boldsymbol{c}'(s)$, the relations

$$\mathbb{A}_f[\boldsymbol{I}] = \boldsymbol{A}_f \quad \text{and} \quad \operatorname{tr}\left(\boldsymbol{A}_f\right) = 1 \tag{2.5}$$

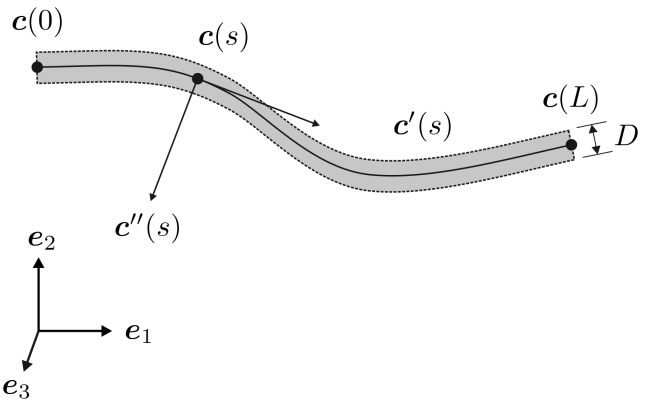

FIGURE 2 | Twice continuously differentiable curve parametrized by arc length.

hold. As the fiber orientation tensor of the second order is symmetric, the tensor may be diagonalized

$$\boldsymbol{A}_f \hat{=} \operatorname{diag}\left(a_1, a_2, a_3\right) \tag{2.6}$$

by a rotation into the eigenbasis, where we use the ordering convention

$$a_3 \le a_2 \le a_1 \tag{2.7}$$

for convenience. The eigenvalues are constrained by the condition,

$$a_1 + a_2 + a_3 = 1 \tag{2.8}$$

a reformulation of Equation (2.5), and are non-negative because the fiber orientation tensor is positive semi-definite by Equation (2.4).

As a consequence of Equation (2.8), the fiber orientation tensor of second order is completely determined by two eigenvalues, for example, a_1 and a_2. With the ordering convention (2.7), the two-dimensional configuration space of the fiber orientation tensor of second order may be visualized by the *fiber orientation triangle* [50, 51], see Figure 3. The vertices mark the three extreme fiber orientation states, namely the isotropic state ($a_i = 1/3$, $i = 1, 2, 3$), the planar isotropic state ($a_1 = a_2 = 1/2, a_3 = 0$) and the unidirectional state ($a_1 = 1, a_2 = a_3 = 0$).

Whereas short fibers are accurately modeled by straight cylinders, longer fibers require taking the fiber curvature into account. Classically, the curvature [52, 53] of a curve (2.1) parametrized by arc length is defined via

$$\kappa(s) = \|\boldsymbol{c}''(s)\|, \quad s \in [0, L] \tag{2.9}$$

With the goal of generating suitable fiber microstructures in mind, we would like to prescribe a suitable statistical measure of fiber curvature. However, this quest is not straightforward, for a number of reasons. For a start, the fiber orientation and the fiber curvature are not independent. Suppose, for instance, that the fiber orientation state is unidirectional, that is, described by the fiber orientation tensor

$$\boldsymbol{A} = \boldsymbol{p} \otimes \boldsymbol{p} \tag{2.10}$$

for some unit vector $\boldsymbol{p}$. Then, all fibers need to be straight and point in direction $\pm\boldsymbol{p}$, see Schneider [54, 3.2.2]. In particular, the curvature $\boldsymbol{c}'' \equiv \boldsymbol{0}$ needs to vanish for all fibers. The average curvature

$$\overline{\kappa}_f = \frac{1}{L}\int_0^L \|\boldsymbol{c}''(s)\|\, ds \tag{2.11}$$

serves as an educated guess for a curvature measure, but does not turn out to be robust with respect to the discretization of the fibers as polygonal chains, see Section 2.2.

As a convenient alternative for quantifying the fiber curvature, we consider the deviation from straight curve (DSC). The latter computes as the trace of the local second-order fiber orientation tensor's covariance for a single fiber

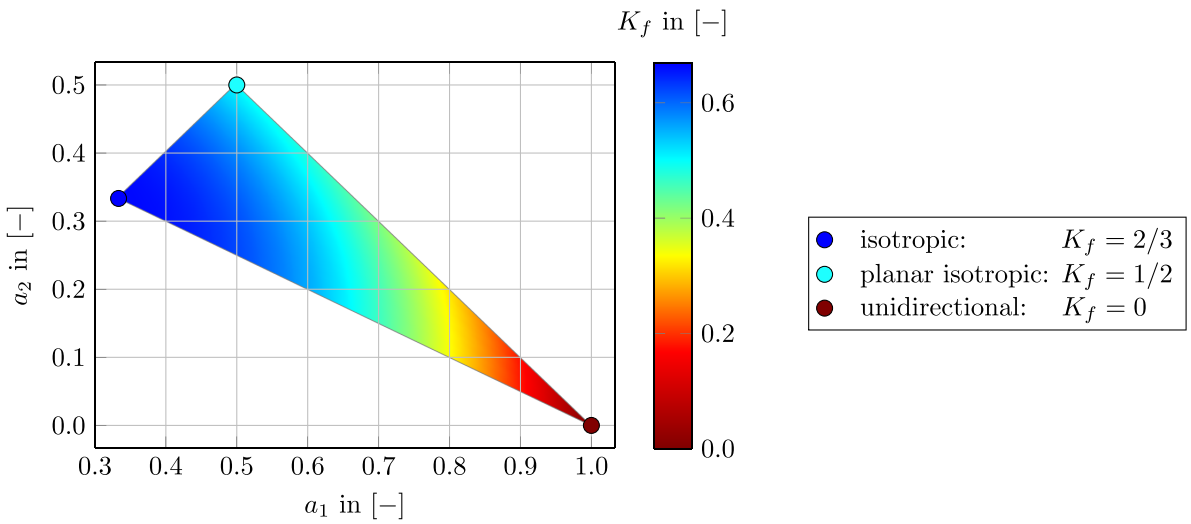

FIGURE 3 | Fiber orientation triangle with the corresponding values of the deviation from straight curve K_f (2.18).

$$K_f \equiv \operatorname{tr}\left(\frac{1}{L}\int_0^L \left(\boldsymbol{A}_f - \boldsymbol{c}'(s)\otimes\boldsymbol{c}'(s)\right)^{\otimes 2}\, ds\right) \tag{2.12}$$

which we may reformulate to

$$K_f = \frac{1}{L}\int_0^L \|\boldsymbol{A}_f - \boldsymbol{c}'(s)\otimes\boldsymbol{c}'(s)\|^2\, ds \tag{2.13}$$

This measure comes with a number of favorable properties.

1. The DSC is non-negative and vanishes only for straight fibers. More precisely, the bounds

$$0 \le K_f \le \frac{2}{3} \tag{2.14}$$

hold, and we have the characterization

$$K_f = 0 \quad \text{if and only if} \quad \boldsymbol{c}''(s) = \boldsymbol{0} \quad \text{for all} \quad s \in [0, L] \tag{2.15}$$

2. The DSC serves as a lower bound to the average curvature in the sense that the inequality

$$K_f \le 2\left(L\,\overline{\kappa}_f\right)^2 \tag{2.16}$$

holds.

3. The DSC admits the equivalent representation

$$K_f = 1 - \|\boldsymbol{A}_f\|^2 \tag{2.17}$$

in terms of the second-order fiber orientation tensor (2.4). Assuming that the fiber orientation tensor of second order is given in its diagonalized form (2.6), the DSC may be computed with two of the three eigenvalues, for example,

$$K_f = 1 - \left(a_1^2 + a_2^2 + a_3^2\right) = 1 - \left(a_1^2 + a_2^2 + \left(1 - a_1 - a_2\right)^2\right) \tag{2.18}$$

where the configuration space of the DSC is given by the points on the fiber orientation triangle. The values of the DSC are shown in Figure 3. We observe that the value 2/3 is only obtained in the case of an isotropic fiber orientation state.

The first property (2.14) and (2.15) enables us to use the DSC as a curvature measure, that is, to quantify the deviation of the curve from being straight. The second property (2.16) relates the DSC to more classical measures of curvature. In particular, a positive value of the DSC enforces the average curvature to be positive, as well. Last but not least, the expression (2.17) is convenient for calculating the DSC in practice.

Establishing the validity of these statements is straightforward. For the convenience of the reader, the derivations are included in Appendix A.

2.2 | Discretization of the Curved Fibers

We discretize the twice continuously differentiable curve $\boldsymbol{c}$ describing a curved fiber as a polygonal chain [33]. The polygonal chain consists of n spherocylinders, that is, cylinders with hemispheres at their ends, as segments, which have the uniform segment length $\ell = L/n$ and the diameter D. Following Lauff et al. [41], we parametrize the polygonal chain with the starting point $\mathbf{x}^0$ in the normalized form

$$\hat{\mathbf{x}}^0 = \hat{\mathbf{Q}}^{-1}\,\mathbf{x}^0 \quad \text{with the matrix} \quad \hat{\mathbf{Q}} = \operatorname{diag}(Q_1, Q_2, Q_3) \tag{2.19}$$

and the directions of the segments $\mathbf{p}^a \in S^2$ $(a = 1, \ldots, n)$. The normalized starting point $\hat{\mathbf{x}}^0$ and the directions $\mathbf{p}^a$ are collected in the coordinate vector

$$\mathbf{q} = \left[\left(\hat{\mathbf{x}}^0\right)^{\mathrm{T}} \left(\mathbf{p}^1\right)^{\mathrm{T}} \cdots \left(\mathbf{p}^n\right)^{\mathrm{T}}\right]^{\mathrm{T}} \tag{2.20}$$

with the dimension

$$n_q = 3\,(n+1) \tag{2.21}$$

to describe a polygonal chain in vector-valued form. As the directions need to be normalized, the admissible configuration space of a curved fiber reads

$$\mathcal{R} = \left\{ \mathbf{q} \in \mathbb{R}^{n_q} \,\middle|\, \boldsymbol{\Phi}_1(\mathbf{q}) = \mathbf{0} \right\} \tag{2.22}$$

with the n-dimensional vector-valued constraint function

$$\boldsymbol{\Phi}_1(\mathbf{q}) = \left[\Phi_1^1(\mathbf{q}) \ \cdots \ \Phi_1^n(\mathbf{q}) \right]^{\mathrm{T}}$$
$$\text{with} \quad \Phi_1^a(\mathbf{q}) = \frac{1}{2}\left(\|\mathbf{p}^a\|^2 - 1 \right), \quad a = 1, \ldots, n \tag{2.23}$$

The discretization as a polygonal chain and the parametrization with the coordinate vector $\mathbf{q}$ are visualized in Figure 4.

Based on this discretization, the local curvature (2.9) at the connection point of the a^{th} and the $(a+1)^{\text{th}}$ segment may be approximated by finite differences [33]

$$\kappa^a \equiv \frac{\|\mathbf{p}^{a+1} - \mathbf{p}^a\|}{\ell}, \quad a = 1, \ldots, n-1 \tag{2.24}$$

which we rewrite as

$$\kappa^a = \frac{\sqrt{2(1 - \mathbf{p}^a \cdot \mathbf{p}^{a+1})}}{\ell}, \quad a = 1, \ldots, n-1 \tag{2.25}$$

using the normalization condition of the directions. In terms of the angle α^a between the a^{th} and the $(a+1)^{\text{th}}$ segments, see Figure 4b, the expression (2.25) may be reformulated

$$\kappa^a = \frac{\sqrt{2(1 - \cos\alpha^a)}}{\ell}, \quad a = 1, \ldots, n-1 \tag{2.26}$$

For the discretized curve, the fiber orientation tensors of second order and fourth order are computed as

$$\boldsymbol{A}_f = \frac{1}{n}\sum_{a=1}^{n} \boldsymbol{p}^a \otimes \boldsymbol{p}^a \quad \text{as well as} \quad \mathbb{A}_f = \frac{1}{n}\sum_{a=1}^{n} \boldsymbol{p}^{\otimes 4} \tag{2.27}$$

and the DSC is computed with the formula

$$K_f = \frac{1}{n}\sum_{a=1}^{n} \|\boldsymbol{A}_f - \boldsymbol{p}^a \otimes \boldsymbol{p}^a\|^2 = 1 - \|\boldsymbol{A}_f\|^2 \tag{2.28}$$

In Figure 5, single fibers discretized as polygonal chains with the DSCs $K_f = 0$, $K_f = 1/3$ and $K_f = 2/3$ are shown. As the fiber lengths exceed the selected cell size, the fibers wrap around the periodic cell multiple times. In accordance with our previous discussion, the selection of the DSC to be $K_f = 0$ leads to straight fibers, that is, no fiber curvature is realized, see Figure 5a. With increasing DSC, we observe that the degree of curvature of the

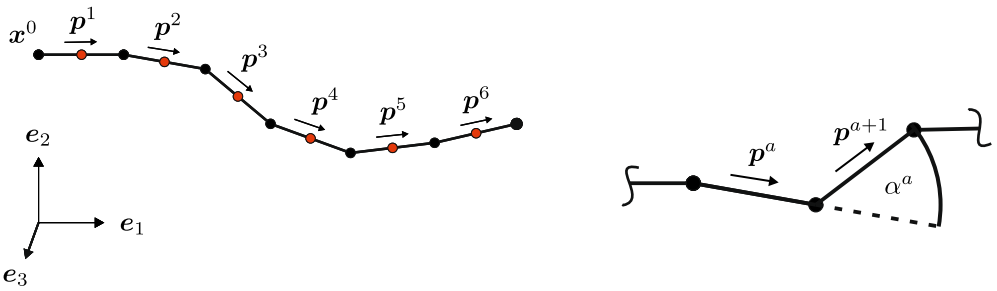

(a) Discretization as a polygonal chain (b) Angle α^a

FIGURE 4 | Discretization of the twice continuously differentiable curve as a polygonal chain (a) and the angle α^a between the a^{th} and the $(a+1)^{\text{th}}$ segments (b).

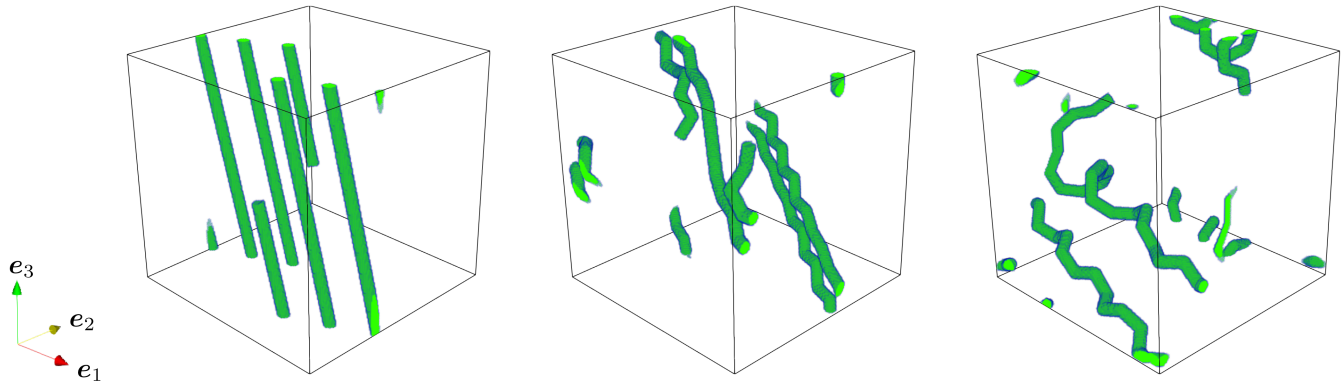

(a) $K_f = 0$ (b) $K_f = \frac{1}{3}$ (c) $K_f = \frac{2}{3}$

FIGURE 5 | Cells filled with single fibers and varying deviations from straight curve K_f.

fibers is also increasing, see Figure 5b,c. For $K_f = 2/3$, the highest degree of curvature is realized. As the DSC only takes the value $2/3$ for the extreme case of an isotropic fiber orientation state, the fiber is formed as a three-dimensional spiral.

3 | Generating Microstructures Filled With Curved Fibers

3.1 | Description of Fiber-Reinforced Composites With Long and Curved Fibers

We consider a periodic unit cell $Q = [0, Q_1] \times [0, Q_2] \times [0, Q_3]$ which should contain N curved fibers in a non-overlapping configuration. The fibers have a uniform fiber diameter D and their centerline is described by polygonal chains, see Section 2.2. For the parametrization of the polygonal chain describing the i^{th}-fiber ($i = 1, \ldots, N$), we use the coordinate vector $\mathbf{q}_i$ (2.20). The fiber lengths L_i are described in terms of a fiber length distribution, for example, the Dirac, the Weibull, or the log-normal distribution. A prescribed maximum segment length $\overline{\ell}$ is used to select the number of segments for each fiber, depending on the fiber length L_i

$$n_i = \left\lceil \frac{L_i}{\overline{\ell}} \right\rceil, \quad \ell_i = \frac{L_i}{n_i}, \quad i = 1, \ldots, N \tag{3.1}$$

where the bracket $\lceil \cdot \rceil$ denotes the ceiling function, that is, the smallest integer larger than the input real number. Due to the non-penetrating fiber arrangement, the total fiber volume fraction is computed as the sum of the fiber volume fraction of the single fibers

$$\phi = \frac{\pi L_{\text{total}} D^2}{4 Q_1 Q_2 Q_3} \tag{3.2}$$

where

$$L_{\text{total}} = \sum_{i=1}^{N} L_i \tag{3.3}$$

denotes the total fiber length. The volume-weighted fiber orientation tensors of the second order and the fourth order are computed as

$$\boldsymbol{A} = \frac{1}{L_{\text{total}}} \sum_{i=1}^{N} L_i \, \boldsymbol{A}_f^i \quad \text{and} \quad \mathbb{A} = \frac{1}{L_{\text{total}}} \sum_{i=1}^{N} L_i \mathbb{A}_f^i \tag{3.4}$$

where $\boldsymbol{A}_f^i$ and $\mathbb{A}_f^i$ are the fiber orientation tensors (2.27) of the i^{th}-fiber.

The information on the fiber orientation state of fiber-reinforced composites is typically obtained from micro-CT imaging [8, 36, 45, 55–57] or from filling simulations [1, 58, 59]. Whereas from micro-CT imaging, also the fiber orientation tensors of higher orders may be extracted, filling simulations typically only provide the fiber orientation tensor of second order $\boldsymbol{A}$. However, to estimate the effective elastic stiffness, fiber orientation tensors of higher order are required as they include additional information [60, 61]. Based on a given second-order fiber orientation tensor, the required fiber orientation tensors of higher order may be approximated by closures [39, 50, 62–65]

$$\mathbb{A} = \mathbb{F}(\boldsymbol{A}). \tag{3.5}$$

However, such approaches do not provide a fiber orientation distribution, which is required to sample fiber directions, for example, during the microstructure generation. Thus, alternative approaches, for example, the exact (ACG) closure [66, 67] or the maximum entropy closure [60, 68], first approximate the fiber orientation distribution and subsequently compute the desired fiber orientation tensors from the fiber orientation distribution. In this manuscript, we use the exact closure to obtain an approximation for the fiber orientation distribution as well as for the fiber orientation tensor of fourth order.

Additionally, the volume-weighted DSC is introduced as

$$\overline{K} = \frac{1}{L_{\text{total}}} \sum_{i=1}^{N} L_i \, K_f^i \tag{3.6}$$

where K_f^i denotes the DSC (2.28) of the i^{th}-fiber. Due to the non-negativity of the lengths L_i and the range of the parameter K_f^i (2.14), the volume-weighted DSC also satisfies the bounds

$$0 \leq \overline{K} \leq \frac{2}{3} \tag{3.7}$$

To prevent excessively high fiber bending, we require that the approximated curvatures κ_i^a (2.26) between two adjacent segments do not exceed a predefined maximum curvature $\overline{\kappa}$

$$\kappa_i^a \leq \overline{\kappa}, \quad i = 1, \ldots, N, \quad a = 1, \ldots, n_i - 1 \tag{3.8}$$

3.2 | Objective Function With Extended Curvature Control

According to the core procedure of the fused sequential addition and migration (fSAM) method [41, 42], we use an optimization algorithm to find admissible fiber arrangements. Therefore, we introduce a non-negative objective function F such that all fiber configurations characterized by the roots of the objective function

$$F(\mathbf{f}_1, \ldots, \mathbf{f}_N) = 0 \tag{3.9}$$

are admissible solutions of the optimization problem. The vector $\mathbf{f}_i$ is an alternative parametrization of the i^{th}-fiber comprising the midpoints $\mathbf{x}_i^a$ and direction $\mathbf{p}_i^a$ of all segments

$$\mathbf{f}_i = \left[(\mathbf{x}_i^1)^{\mathrm{T}} \ \cdots \ (\mathbf{x}_i^{n_i})^{\mathrm{T}} \ (\mathbf{p}_i^1)^{\mathrm{T}} \ \cdots \ (\mathbf{p}_i^{n_i})^{\mathrm{T}} \right]^{\mathrm{T}} \tag{3.10}$$

With a given coordinate vector $\mathbf{q}_i$, the midpoints of the segments may be computed as

$$\mathbf{x}_i^a(\mathbf{q}_i) = \hat{\mathbf{Q}} \, \hat{\mathbf{x}}_i^0 + \sum_{b=1}^{a-1} \ell \, \mathbf{p}_i^b + \frac{\ell}{2} \mathbf{p}_i^a, \quad a = 1, \ldots, n_i \tag{3.11}$$

The original objective function of the fSAM algorithm [41] includes only a maximum angle constraint to prevent excessively high kinks between adjacent segments. However, prescribing a desired degree of fiber curvature is not possible. Thus, we aim to extend the objective function by a term taking the desired

volume-weighted DSC $\overline{K}$ into account. More precisely, we aim to satisfy the non-overlap condition, the maximum curvature constraint (3.8), as well as the desired fiber orientation and curvature states

$$\mathbb{A} \stackrel{!}{=} \mathbb{A}^r \quad \text{and} \quad \overline{K} \stackrel{!}{=} \overline{K}^r \tag{3.12}$$

where we distinguish between the desired states $\mathbb{A}$ or $\overline{K}$ and the currently realized states $\mathbb{A}^r$ or $\overline{K}^r$.

We start the discussion with the introduction of the objective function [33, 41] of dimension (length)^2

$$F(\mathbf{f}_1, \ldots, \mathbf{f}_N) \;\hat{=}\; \frac{1}{2}\sum_{i,j=1}^{N}\sum_{a=1}^{n_i}\sum_{b=1}^{n_j}\left(\delta_{ij}^{ab}\right)^2 + \frac{w_{\mathbb{A}}}{8}\, N\, \|\mathbb{A} - \mathbb{A}^r\|^2 \tag{3.13}$$

including a term for the non-overlap condition and the fiber orientation tensor of fourth order. The non-overlap condition is characterized by the quantity

$$\begin{aligned}\delta_{ij}^{ab} &\equiv \left\langle D - \min_{s_i^a, s_j^b \in [-1,1]} d_Q\left(\boldsymbol{x}_i^a + s_i^a\,\frac{\ell_i}{2}\,\boldsymbol{p}_i^a, \boldsymbol{x}_j^b + s_j^b\,\frac{\ell_j}{2}\,\boldsymbol{p}_j^b\right)\right\rangle_+ \\ &\equiv \langle D - \|\boldsymbol{k}_{ij}^{ab}\|\rangle_+ \end{aligned} \tag{3.14}$$

using the vector $\boldsymbol{k}_{ab}^{ij}$ to denote the smallest periodic distance between two segments and expressing the Macaulay bracket with $\langle h\rangle_+ = \max(0, h)$. Whereas the term for the non-overlap condition is considered until a non-penetrating arrangement is found, the fiber orientation term is only active if the convergence criterion

$$\frac{\|\mathbb{A} - \mathbb{A}^r\|}{\|\mathbb{A}\|} \le \epsilon_{\mathbb{A}} \tag{3.15}$$

with the tolerance $\epsilon_{\mathbb{A}}$ does not hold. The weight $w_{\mathbb{A}}$ for the orientation term [41] is selected as

$$w_{\mathbb{A}} \equiv \varepsilon(\ell_i, D)\frac{\varepsilon(n_i\,\ell_i, D)}{n_i\,\varepsilon(\ell_i, D)} = \frac{\varepsilon(n_i\,\ell_i, D)}{n_i} \tag{3.16}$$

with the volume-specific moment of inertia of a spherocylinder [69]

$$\varepsilon(\ell_i, D) = \frac{D^2}{2/3 + \ell_i/D}\left[\frac{(\ell_i/D)^3}{12} + \frac{(\ell_i/D)^2}{6} + \frac{3\,\ell_i/D}{16} + \frac{1}{15}\right] \tag{3.17}$$

To account for the desired volume-weighted DSC $\overline{K}$ (3.6) and the maximum curvature constraint (3.8), we extend the objective function by two additional terms

$$\begin{aligned} F_{\text{curvature}}(\mathbf{f}_1, \ldots, \mathbf{f}_N) \;\hat{=}\; & \frac{1}{2}\sum_{i,j=1}^{N}\sum_{a=1}^{n_i}\sum_{b=1}^{n_j}\left(\delta_{ij}^{ab}\right)^2 \\ & + \frac{w_{\mathbb{A}}}{8}\, N\, \|\mathbb{A} - \mathbb{A}^r\|^2 \\ & + \frac{w_{\overline{K}}}{8}\, n_s\, \left(\overline{K} - \overline{K}^r\right)^2 \\ & + \frac{w_{\overline{\kappa}}\,\ell_{\text{mean}}^4}{2}\sum_{i=1}^{N}\sum_{a=1}^{n_i-1}\left(\left\langle \left(\kappa_i^a\right)^2 - \overline{\kappa}^2\right\rangle_+\right)^2 \end{aligned} \tag{3.18}$$

The third term accounts for the desired volume-weighted DSC $\overline{K}$ with the empirical weight $w_{\overline{K}} = 20\; w_{\boldsymbol{A}}$. The maximum curvature constraint is realized by the fourth term, where the mean segment length is computed as

$$\ell_{\text{mean}} = \frac{L_{\text{total}}}{n_s} \quad \text{with} \quad n_s = \sum_{i=1}^{N} n_i \tag{3.19}$$

and we choose the weight to be $w_{\overline{\kappa}} = 1.5\;\varepsilon(\ell_i, D)$. Within the objective function $F_{\text{curvature}}$ (3.18), the terms for the desired fiber curvature parameter and the maximum angle constraint are taken into account via the convergence criteria

$$\begin{aligned} &\frac{\|\overline{K} - \overline{K}^r\|}{\overline{K}} \le \epsilon_{\overline{K}} \quad \text{and} \\ &\frac{\left\langle \kappa_i^a - \overline{\kappa}\right\rangle_+}{\overline{\kappa}} \le \epsilon_{\overline{\kappa}}, \quad i = 1, \ldots, N, \quad a = 1, \ldots, n_i - 1 \end{aligned} \tag{3.20}$$

respectively. The convergence criterion for the maximum curvature constraint is evaluated for all adjacent segments individually. In case of a desired DSC $\overline{K}$, the weights for the fiber orientation term $w_{\boldsymbol{A}}$ and for the maximum curvature constraint $w_{\overline{\kappa}}$ need to be increased, and we select a factor of two for both weights. Selecting the weights for the individual terms within the objective function to ensure a stable convergence behavior of the algorithm is critical. We selected the weights by trial and error, investigating numerous different combinations of microstructural descriptors to ensure that the weighting factors work for a wide range of desired microstructures. In fact, the algorithm is quite sensitive with respect to the selection of the weighting factors, underlining the importance of an adequate choice.

For the optimization procedure of the fSAM algorithm [41], the directional derivatives of the objective function with respect to the coordinate vector $\mathbf{f}_i$ are necessary. According to the extended objective function $F_{\text{curvature}}$ (3.18), the directional derivatives compute as

$$\begin{aligned} \frac{\partial F_{\text{curvature}}(\mathbf{f}_1, \ldots, \mathbf{f}_N)}{\partial \mathbf{x}_i^a} &\;\hat{=}\; -\sum_{j=1}^{N}\sum_{b=1}^{n_j}\delta_{ij}^{ab}\,\frac{\boldsymbol{k}_{ij}^{ab}}{\left\|\boldsymbol{k}_{ij}^{ab}\right\|} \\ \frac{\partial F_{\text{curvature}}(\mathbf{f}_1, \ldots, \mathbf{f}_N)}{\partial \mathbf{p}_i^a} &\;\hat{=}\; -\sum_{j=1}^{N}\sum_{b=1}^{n_j}\delta_{ij}^{ab}\,\frac{\ell_i\; s_{ij}^{ab}}{2}\,\frac{\boldsymbol{k}_{ij}^{ab}}{\left\|\boldsymbol{k}_{ij}^{ab}\right\|} \\ & \quad - w_{\mathbb{A}}\,\frac{\ell_i\, N}{L_{\text{total}}}(\mathbb{A} - \mathbb{A}^r)\left[(\boldsymbol{p}_i^a)^{\otimes 3}\right] \\ & \quad + w_{\overline{K}}\,\frac{\ell_i}{\ell_{\text{mean}}}\left(\overline{K} - \overline{K}^r\right)\boldsymbol{A}_f^i\;\boldsymbol{p}_i^a \\ & \quad - w_{\overline{\kappa}}\,\frac{2\,\ell_{\text{mean}}^4}{\ell_i^2}\left(\left\langle \left(\kappa_i^a\right)^2 - \overline{\kappa}^2\right\rangle_+\boldsymbol{p}_i^{a+1}\right. \\ & \quad \left. + \left\langle \left(\kappa_i^{a-1}\right)^2 - \overline{\kappa}^2\right\rangle_+\boldsymbol{p}_i^{a-1}\right) \end{aligned} \tag{3.21}$$

3.3 | Optimization Procedure of the Fused Sequential Addition and Migration Method

To solve the optimization problem

$$F(\mathbf{f}_1, \ldots, \mathbf{f}_N) \to \min_{\mathbf{q}_i \in \mathcal{R}_i} \tag{3.22}$$

we use a gradient descent approach parametrized by the coordinate vectors $\mathbf{q}_i$. The iterates are restricted to the curved, that is, non-flat, configuration space $\mathcal{R}_i$ (2.22). Thus, a basic descent gradient approach may leave the admissible configuration space. To ensure a motion on the optimization space, we apply an adapted gradient descent approach [41, 42] moving along the geodesics, that is, the shortest line between two points on the curved manifold. Then, the iterates of the optimization problem are computed as

$$\mathbf{q}_i^{k+1} = \exp_{\mathbf{q}_i^k}\left(-\tau\ \nabla_{\mathbf{q}_i} F\left(\mathbf{f}_1^k, \ldots, \mathbf{f}_N^k\right)\right), \quad k = 0, 1, \ldots \tag{3.23}$$

with the stepsize τ, the gradient of the objective function $\nabla_{\mathbf{q}_i} F\left(\mathbf{f}_1^k, \ldots, \mathbf{f}_N^k\right)$ with respect to the coordinate vector $\mathbf{q}_i$ and the exponential mapping $\exp_{\mathbf{q}}(\mathbf{v})$. Detailed information on the equations governing the geodesics of the considered polygonal chain, as well as on the adapted gradient descent approach, see Equation (3.23), is given in Appendix B.

To obtain the gradient of the objective function $\nabla_{\mathbf{q}_i} F\left(\mathbf{f}_1^k, \ldots, \mathbf{f}_N^k\right)$ with respect to the coordinate vector $\mathbf{q}_i$, we apply the chain rule and follow the procedure introduced by Lauff et al. [41]: As the objective function $F\left(\mathbf{f}_1, \ldots, \mathbf{f}_N\right)$ is defined in terms of the midpoints and the directions collected in the coordinate vectors $\mathbf{f}_i$, we first compute the directional derivatives with respect to the midpoints and directions $\partial F\left(\mathbf{f}_1, \ldots, \mathbf{f}_N\right)/\partial \mathbf{x}_i^a$ and $\partial F\left(\mathbf{f}_1, \ldots, \mathbf{f}_N\right)/\partial \mathbf{p}_i^a$. Then, the directional derivatives for the coordinate vectors $\mathbf{q}_i$ are obtained by the relation [41]

$$\begin{aligned}
\frac{\partial F\left(\mathbf{f}_1, \ldots, \mathbf{f}_N\right)}{\partial \mathbf{q}_i} &= \left(\frac{\partial \mathbf{f}_i}{\partial \mathbf{q}_i}\right)^{\mathrm{T}} \frac{\partial F\left(\mathbf{f}_1, \ldots, \mathbf{f}_N\right)}{\partial \mathbf{f}_i} \\
&= \begin{bmatrix} \hat{\mathbf{Q}} \sum_{a=1}^{n_i} \dfrac{\partial F\left(\mathbf{f}_1, \ldots, \mathbf{f}_N\right)}{\partial \mathbf{x}_i^a} \\ R_1\left(\mathbf{f}_1, \ldots, \mathbf{f}_N\right) \\ \vdots \\ R_{n_i}\left(\mathbf{f}_1, \ldots, \mathbf{f}_N\right) \end{bmatrix} \\
\text{with} \quad R_a\left(\mathbf{f}_1, \ldots, \mathbf{f}_N\right) &= F\left(\mathbf{f}_1, \ldots, \mathbf{f}_N\right)\left(\frac{\partial}{\partial \mathbf{p}_i^a} + \sum_{b=a+1}^{n_i} \ell_i \frac{\partial}{\partial \mathbf{x}_i^b} + \frac{\ell_i}{2} \frac{\partial}{\partial \mathbf{x}_i^a}\right)
\end{aligned} \tag{3.24}$$

where $\hat{\mathbf{Q}}$ denotes the normalization matrix for the starting point (2.19) and ℓ_i the segment length. For the curved manifold $\mathcal{R}_i$ (2.22), the gradient is obtained by scaling the directional derivatives by the inverse of the metric matrix [70]

$$\nabla_{\mathbf{q}_i} F\left(\mathbf{f}_1, \ldots, \mathbf{f}_N\right) = \mathbf{G}_i^{-1} \frac{\partial F\left(\mathbf{f}_1, \ldots, \mathbf{f}_N\right)}{\partial \mathbf{q}_i} \tag{3.25}$$

where an explicit expression for the metric matrix $\mathbf{G}_i$ is given in Equation (B4).

For the stepsize of the iteration rule (3.23), we select $\tau_x = 0.501$ [54] for the directional derivatives $\partial F\left(\mathbf{f}_1^k, \ldots, \mathbf{f}_N^k\right)/\partial \mathbf{x}_i^a$ and a smaller stepsize of $\tau_p = 0.3\tau_x$ for the directional derivatives $\partial F\left(\mathbf{f}_1^k, \ldots, \mathbf{f}_N^k\right)/\partial \mathbf{p}_i^a$. Thus, translation is favored over rotation during the optimization procedure. The optimization procedure of the fSAM algorithm is summarized with the pseudo-code in Algorithm 1.

ALGORITHM 1 | Single optimization step of the fSAM algorithm, taken from Lauff et al. [41].

Input: Coordinate vector $\mathbf{q}_i^k, \quad i = 1, \ldots, N$

Compute the coordinate vectors $\mathbf{f}_i^k$ ▷ Equations (3.10) and (3.11)

for $i \leftarrow 1$ **to** N **do**

  for $a \leftarrow 1$ **to** n_i **do**

    Compute the directional derivatives $\dfrac{\partial F\left(\mathbf{f}_1^k, \ldots, \mathbf{f}_N^k\right)}{\partial \mathbf{x}_i^a}$ and $\dfrac{\partial F\left(\mathbf{f}_1^k, \ldots, \mathbf{f}_N^k\right)}{\partial \mathbf{p}_i^a}$ ▷ Equation (3.21)

  Compute the directional derivative $\dfrac{\partial F\left(\mathbf{f}_1^k, \ldots, \mathbf{f}_N^k\right)}{\partial \mathbf{q}_i}$ ▷ Equation (3.24)

  Compute the gradient $\nabla_{\mathbf{q}_i} F\left(\mathbf{f}_1^k, \ldots, \mathbf{f}_N^k\right)$ ▷ Equation (3.25)

  Compute the updated coordinate vector $\mathbf{q}_i^{k+1}$ ▷ Equation (3.23)

3.4 | Pre-Optimization Step

The procedure of the fSAM algorithm [41] starts with the sampling of straight fibers, which are described by a single segment [33]. More precisely, the fiber midpoints are distributed uniformly within the unit cell, the fiber directions are sampled from the approximated fiber orientation distribution, and the fiber lengths follow the desired fiber length distribution. After the sampling step, the fibers are segmented into n_i segments following Equation (3.1). Although the sampling of the fiber directions accounts for the desired fiber orientation distribution, the realized fiber orientation state may differ from the desired one as we consider a finite number of fibers. To ensure an adequate fiber orientation state before starting the main optimization procedure, a pre-optimization step is executed, minimizing the objective function without considering the non-overlap condition.

For the extended objective function $F_{\text{curvature}}$ (3.18), the objective function of the pre-optimization step is defined as

$$\begin{aligned}
F_{\text{pre},1}\left(\mathbf{f}_1, \ldots, \mathbf{f}_N\right) \hat{=}\ & \frac{w_{\mathbb{A}}}{8}\ N\ \|\mathbb{A} - \mathbb{A}^r\|^2 \\
& + \frac{w_{\overline{K}}}{8}\ n_s \left(\overline{K} - \overline{K}^r\right)^2 \\
& + \frac{w_{\overline{\kappa}}\ \ell_{\text{mean}}^4}{2} \sum_{i=1}^{N} \sum_{a=1}^{n_i - 1} \left(\left\langle \left(\kappa_i^a\right)^2 - \overline{\kappa}^2 \right\rangle_+\right)^2
\end{aligned} \tag{3.26}$$

dropping the term for the non-overlap condition. However, in our studies, it turned out that the pre-optimization step with already segmented fibers leads to drastically increased runtimes for the main optimization procedure when prescribing small volume-weighted DSCs. To improve the efficiency of the algorithm, we use straight fibers with a single segment for the pre-optimization step and subsequently conduct the decomposition into n_i segments. For this alternative approach, the objective function reads

$$F_{\text{pre},2}\left(\mathbf{f}_1, \ldots, \mathbf{f}_N\right) \hat{=}\ \frac{w_{\mathbb{A}}}{8}\ N\ \|\mathbb{A} - \mathbb{A}^r\|^2 \tag{3.27}$$

Compared to the original formulation (3.26), two terms are missing. As the fibers are straight, the realized volume-weighted DSC $\overline{K}^r$ equals zero, and we take the desired DSC $\overline{K}$ into consideration once the main optimization starts. Furthermore, the maximum curvature constraint is intrinsically ensured as the local curvature of the fiber vanishes.

The decision to use straight fibers for the pre-optimization step enables the microstructure generation for small DSCs, that is, almost straight fibers. In addition, in our studies, it turned out that the generation time for higher fiber curvatures is not influenced significantly by this choice. With respect to the generated fibers within the final microstructure, the pre-optimization step with straight fibers may lead to smaller mean values of the local fiber curvature. However, at this point, generating microstructures for a wide range of DSCs is only possible efficiently when making the algorithmic choice of straight fibers in the pre-optimization step.

4 | Computational Investigations

4.1 | Setup

The fSAM algorithm is written in Python with Cython extensions and partly parallelized with OpenMP. The numerical studies were conducted on a desktop computer with an 8-core Intel i7 CPU and 64GB of RAM.

As the reference material system, we use an E-glass fiber reinforced polypropylene (PP) matrix with the elastic constants listed in Table 1.

We consider the fiber diameter $D = 10\mu$m and the fiber length $L = 1000\mu$m, that is, a fiber aspect ratio of $r_a = 100$. The composite has a fiber volume fraction of $\phi = 20\%$. For the fiber orientation tensor of second order, we prescribe $\boldsymbol{A} = \mathrm{diag}(0.75, 0.15, 0.1)$ and approximate the fiber orientation tensor of fourth order with the ACG closure. Thus, the fiber orientation tensor of fourth order is orthotropic [51, 61] and reads

$$\hat{\mathbb{A}} = \begin{bmatrix} 0.6514 & 0.0584 & 0.0402 & 0 & 0 & 0 \\ 0.0584 & 0.0733 & 0.0182 & 0 & 0 & 0 \\ 0.0402 & 0.0182 & 0.0416 & 0 & 0 & 0 \\ 0 & 0 & 0 & 0.0182 & 0 & 0 \\ 0 & 0 & 0 & 0 & 0.0402 & 0 \\ 0 & 0 & 0 & 0 & 0 & 0.0584 \end{bmatrix} \tag{4.1}$$

in Voigt's notation. Furthermore, we choose the maximum curvature $\overline{\kappa} = 0.021/\mu m$, that is, in case of the segment lengths $\ell = 40\mu$m, 25μm and 15μm, the maximum angle $\overline{\alpha}$ between adjacent segments is about 47°, 29°, and 17°, respectively. The maximum segment length $\overline{\ell}$ and the desired volume-weighted DSC $\overline{K}$ are selected in the individual studies.

TABLE 1 | Isotropic elastic moduli for the PP matrix and the E-glass fibers [71–73].

E-glass fibers	PP matrix
$E = 72.0$ GPa	$E = 1.25$ GPa
$\nu = 0.22$	$\nu = 0.35$

As an algorithmic choice, we select a minimum distance between the fibers of 20% of the fiber diameter, that is, 2.0μm. Additionally, we insist that the relative error of the fiber orientation tensor needs to be below $\epsilon_{\mathbb{A}} = 10^{-4}$. The tolerances for the curvature parameter $\overline{K}$ and the maximum curvature constraint are fixed as $\epsilon_{\overline{K}} = \epsilon_{\overline{\kappa}} = 10^{-3}$. For small maximum segment lengths, the number of segments n may be extremely high. As for each optimization step, linear equations of dimension $3(n+1)$ need to be solved; the original fSAM algorithm slows down [41]. Thus, the fSAM algorithm includes a procedure where each fiber with more than a prescribed maximum segment number $\overline{n}$ is divided into separately moving subchains [41]. The coherence condition between the subchains is taken into consideration by an additional term in the objective function. We use this procedure in case that the maximum segment length $\overline{\ell} = 15\mu$m is selected and choose the maximum segment number to be $\overline{n} = 35$. For convergence, the distance between adjacent subchains needs to be below $10^{-3}D$.

Based on the generated microstructures, we compute the effective linear elastic moduli with an FFT-based computational homogenization software [74, 75]. More precisely, we rely on a staggered grid for the discretization [76] and apply a conjugate gradient solver [77–79]. The iterative procedure stops provided the convergence criterion [80] is below 10^{-5}. To obtain the effective elasticity tensor, we use six linearly independent strain-load cases. As the material law is isotropic and the desired fiber orientation tensor of fourth order is orthotropic, see Equation (4.1), the effective elasticity tensor is orthotropic as well. As the material law is isotropic and the desired fiber orientation tensor of fourth order is orthotropic (see Equation 4.1), the effective elasticity tensor is orthotropic, as well. However, due to the approximate realization of the orthotropic fiber orientation tensor of fourth order, the computed apparent stiffness is not completely orthotropic. Thus, we approximate the effective orthotropic engineering constants from the effective elasticity tensor [81, 82]. In addition, to assess the error induced by the orthotropic approximation, we monitor the approximation error

$$\mathrm{err}_{\mathrm{orth}} = \frac{\|\mathbb{C}^r - \mathbb{C}^r_{\mathrm{orth}}\|}{\|\mathbb{C}^r\|} \cdot 100\% \tag{4.2}$$

where $\mathbb{C}^r$ denotes the realized effective stiffness and $\mathbb{C}^r_{\mathrm{orth}}$ its orthotropic approximation.

4.2 | Resolution Study

To compute the effective elasticity tensor adequately, a sufficiently fine resolution is necessary. However, with decreasing mesh size, the computational effort of the computational homogenization increases, as well. Thus, we aim to use a resolution that is fine enough to provide reliable results but still leads to reasonable runtimes of the algorithm. For the resolution study, we use the reference setup from Section 4.1 and generate cubic microstructures with cell dimensions $Q_i = 400\mu$m. To investigate the necessary resolution for microstructures

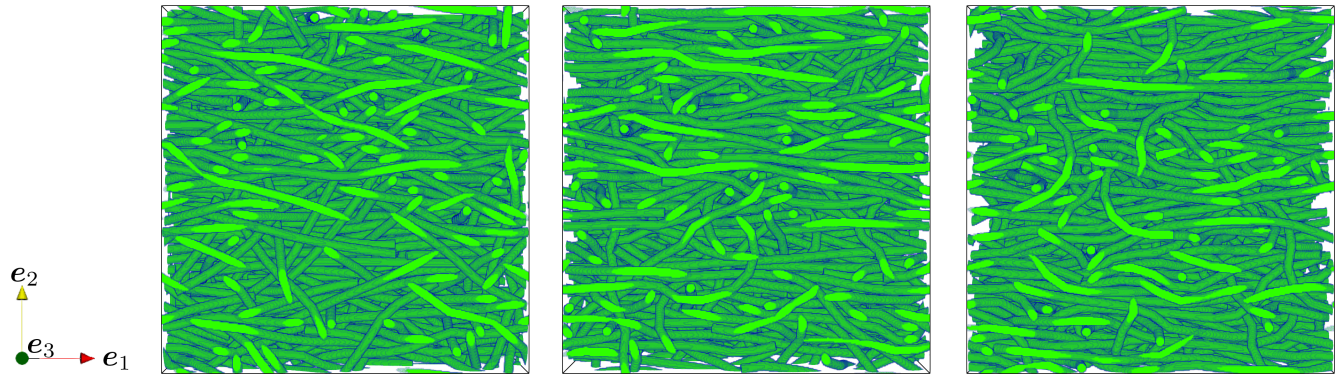

FIGURE 6 | Microstructures with varying volume-weighted deviations from straight curve $\overline{K}$.

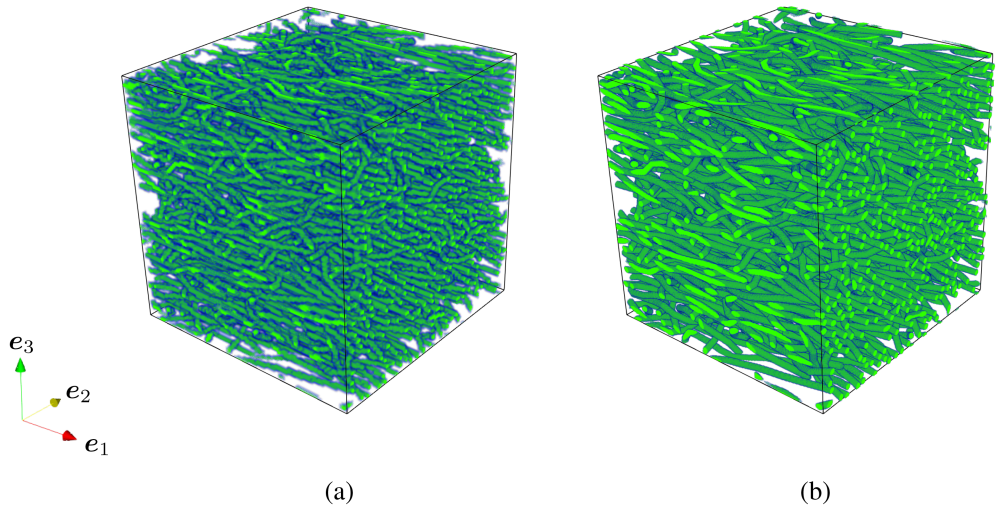

FIGURE 7 | Microstructures with volume-weighted deviation from straight curve $\overline{K} = 0.25$ resolved with the voxel edge-lengths $h = 4.00\mu$m (a) and $h = 1.25\mu$m (b).

with small and high degrees of curvature, we consider the volume-weighted DSC $\overline{K} = 0.06$ and $\overline{K} = 0.25$. Microstructures generated with these volume-weighted DSCs are shown in Figure 6. The maximum segment length is selected as $\overline{\ell} = 25\mu$m, that is, the fibers of length $L = 1000\mu$m are divided into 40 segments.

We study the voxel-edge lengths $h = 1.0\mu$m, 1.25μm, 2.0μm and 4.0μm and show microstructures with the volume-weighted DSC $\overline{K} = 0.25$ for the finest and the coarsest mesh size in Figure 7. Compared to the fiber diameter of $D = 10\mu m$, the selected resolutions have 10, 8, 5, and 2.5 voxels per diameter from the finest to the coarsest mesh size. As the effort for the computational homogenization procedure is mainly driven by the total amount of voxels, which is 400^3, that is, $64 \cdot 10^6$, for the finest resolution and $1 \cdot 10^6$ for the coarsest resolution, the runtime is significantly smaller for the coarser resolution.

TABLE 2 | Approximated orthotropic engineering constants for the voxel edge-lengths $h = 4.00\mu$m, $h = 2.00\mu$m, $h = 1.25\mu$m, and $h = 1.00\mu$m.

$\overline{K}$	h	E_1	E_2	E_3	G_{23}	G_{13}	G_{12}	err_{orth}
—	μm	GPa	GPa	GPa	GPa	GPa	GPa	%
0.06	4.00	7.49	2.60	2.46	0.92	1.15	1.29	3.06
	2.00	8.30	2.59	2.40	0.89	1.13	1.31	1.22
	1.25	8.54	2.60	2.39	0.88	1.12	1.32	0.70
	1.00	8.62	2.60	2.39	0.88	1.13	1.32	0.56
0.25	4.00	6.90	2.47	2.37	0.90	1.07	1.17	2.94
	2.00	7.48	2.40	2.29	0.85	1.02	1.13	1.17
	1.25	7.64	2.38	2.27	0.83	1.01	1.12	0.68
	1.00	7.70	2.38	2.27	0.82	1.00	1.12	0.55

The results of the computations are listed in Table 2. First, we assess the approximation quality of the orthotropic engineering constants from the computed elasticity tensor by computing the approximation error err_{orth}. We observe that the approximation error is above 1% for the two voxel-edge lengths $h = 4\mu$m and 2μm and decreases below 1% for the voxel-edge lengths

$h = 1.25\mu$m and 1μm. Thus, the results demonstrate that the orthotropic approximation is justified. The necessary resolution is chosen by comparing the mechanical properties of the coarser mesh sizes with the results of the finest mesh size. Based on this procedure, we select the coarsest mesh size whose elastic properties only differ with a relative difference below 1% from the finest resolution as the necessary resolution. For the volume-weighted DSC $\overline{K} = 0.06$, the Young's modulus E_1 reveals the highest relative underestimation with 13.11% for the coarsest resolution. With decreasing voxel-edge length, the error reduces to 3.71% for $h = 2\mu$m and 0.93% for $h = 1.25\mu$m. Hence, for small degrees of fiber curvature, the voxel-edge length $h = 1.25\mu$m turns out to be sufficient. With respect to the higher volume-weighted DSC $\overline{K} = 0.25$, the Young's modulus E_1 is also most affected by the resolution. For the coarsest resolution, the relative underestimation is 10.39%, dropping to 2.86% and 0.78% with refining mesh size. As the voxel-edge length $h = 1.25\mu$m results in relative errors below 1% for both curvature parameters, we use this resolution for the following investigations.

4.3 | RVE Study

In computational homogenization, we analyze the material properties of a microstructure using unit cells. The concept of representativity refers to the ability of specific unit cells to accurately reflect the material's *effective* properties, which are the deterministic macroscopic properties that emerge as the volume of the unit cell tends to infinity [14, 83, 84]. On finite-sized unit cells, the computed *apparent* properties are random due to the inherent randomness in the microstructure, that is, they vary for different realizations. As the size of the unit cell increases, the apparent properties converge to the effective properties almost surely, reducing the randomness in the computed values. In this context, a *representative volume element* (RVE) is a unit cell large enough such that its apparent properties closely match the effective properties of the material. To reduce the effort of the computational homogenization, the smallest RVE size should be used. In the context of microstructure generation, periodic geometries in combination with accurately realized descriptors, for example, the fiber volume fraction and fiber orientation tensor of fourth order, enable a reduction of the RVE size [30, 33, 41].

The representativity of a unit cell may be assessed by a statistical approach [14, 85], monitoring the *random* and the *systematic* error. The random error, or dispersion, measures the variance of multiple realizations on a fixed unit cell size. With increasing unit cell size, the variance converges to zero, that is, the apparent properties converge to deterministic values. On the other hand, the systematic error, or bias, quantifies the difference between the mean value of the apparent properties for a fixed unit cell and the effective properties. As the effective properties are typically unknown quantities, we compare the mean apparent properties for increasing cell sizes until convergence.

We use the setup from the previous Section 4.2 and study the representativity of the unit cells with cell dimensions $Q_i = 300\mu$m, 400μm, 500μm. We resolve the microstructures with the voxel-edge length $h = 1.25\mu$m, according to the results of the resolution study 4.2. Based on this resolution, the three unit cells contain the voxel numbers listed in Table 3, that is, the largest unit cell comprises about 4.6 times more voxels than the smallest unit cell.

As all three unit cells are rather small compared to the fiber length $L = 1000\mu$m, the fibers are multiple times larger than the edge lengths. Realizations with the three varying unit cell sizes are shown in Figure 8 for the volume-weighted DSC $\overline{K} = 0.25$.

We report on the mean and the standard deviation of the approximated orthotropic engineering constants in Table 4, generating ten realizations for each unit cell size. In all cases, we observe that the orthotropic approximation error is below 1%, that is, the effective elastic material behavior may be considered as orthotropic.

TABLE 3 | Number of voxels for varying cell dimensions Q_i.

Q_i	μm	300	400	500
Voxel number	—	$240^3 \approx 14 \cdot 10^6$	$320^3 \approx 33 \cdot 10^6$	$400^3 = 64 \cdot 10^6$

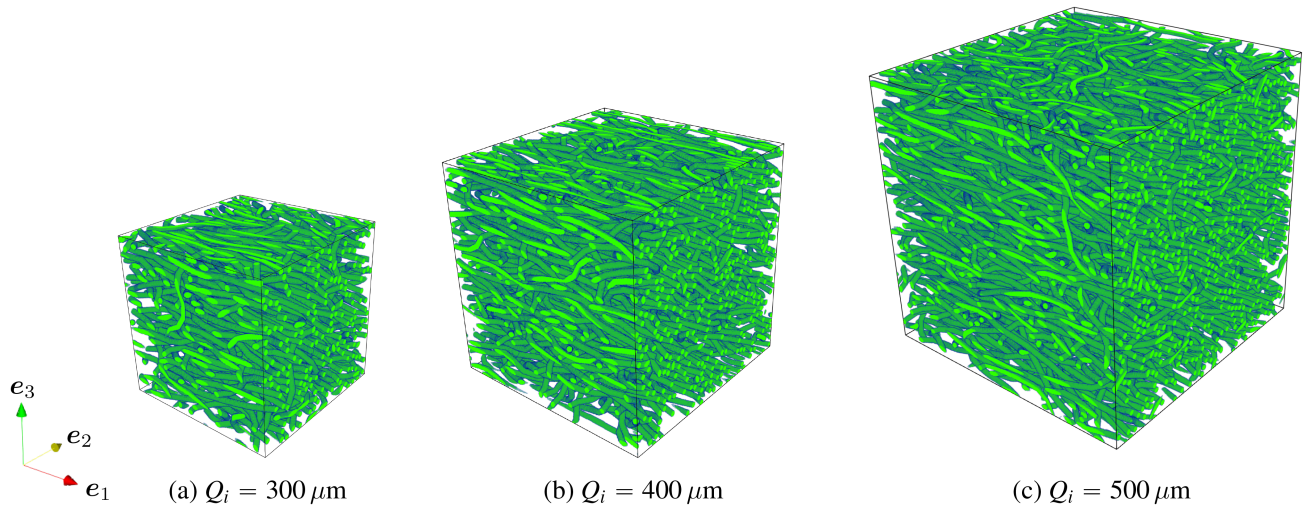

FIGURE 8 | Generated microstructures for three different cubic cell-sizes Q_i.

TABLE 4 | Approximated orthotropic engineering constants for the cubic cell-sizes $Q_i = 300\mu$m, $Q_i = 400\mu$m, and $Q_i = 500\mu$m.

$\overline{K}$	Q_i	E_1	E_2	E_3	G_{23}	G_{13}	G_{12}	$\mathrm{err}_{\mathrm{orth}}$
—	μm	GPa	GPa	GPa	GPa	GPa	GPa	%
0.06	300	8.54 ± 0.03	2.60 ± 0.01	2.39 ± 0.01	0.88 ± 0.00	1.13 ± 0.00	1.32 ± 0.01	0.65 ± 0.09
	400	8.53 ± 0.01	2.60 ± 0.01	2.39 ± 0.00	0.88 ± 0.00	1.13 ± 0.00	1.32 ± 0.00	0.69 ± 0.05
	500	8.52 ± 0.01	2.60 ± 0.00	2.39 ± 0.00	0.88 ± 0.00	1.13 ± 0.00	1.32 ± 0.00	0.68 ± 0.04
0.25	300	7.66 ± 0.03	2.38 ± 0.01	2.27 ± 0.00	0.83 ± 0.00	1.01 ± 0.01	1.12 ± 0.01	0.62 ± 0.07
	400	7.66 ± 0.02	2.38 ± 0.01	2.27 ± 0.00	0.83 ± 0.00	1.01 ± 0.00	1.12 ± 0.00	0.63 ± 0.05
	500	7.65 ± 0.02	2.38 ± 0.00	2.27 ± 0.00	0.83 ± 0.00	1.01 ± 0.00	1.12 ± 0.00	0.59 ± 0.05

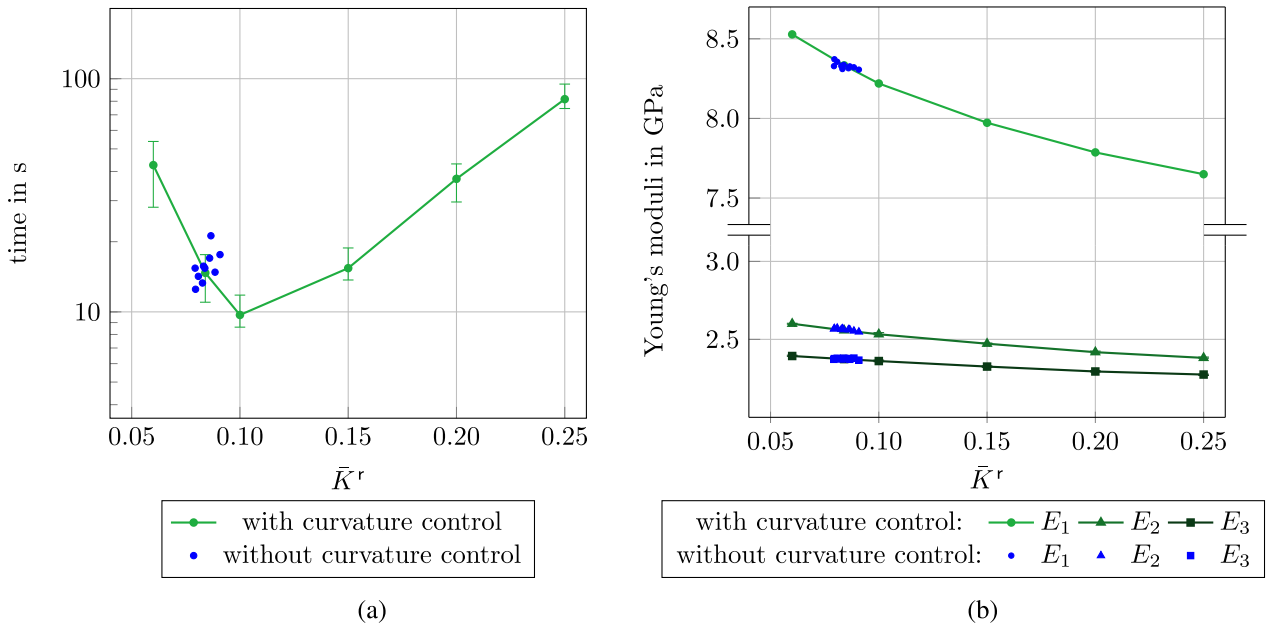

FIGURE 9 | Runtimes for the microstructure generation (a) and the Young's moduli (b) using the fSAM algorithm with or without the curvature control.

With respect to the representativity error, it turns out that both the random and the systematic error only concern the third significant digit. Thus, even the smallest unit cell size may be considered representative for engineering purposes.

As the fiber lengths may exceed the edge-lengths, self-intersection of a fiber needs to be considered when computing the quantity δ_{ij}^{ab}, see Equation (3.14), to characterize the non-overlap condition. As a result, we exclude fiber arrangements that are not admissible due to the resulting self-intersection. An example is a straight fiber in, for example, $\boldsymbol{e}_1$-direction which is longer than the edge-length in $\boldsymbol{e}_1$-direction. Excluding self-intersection gets more challenging the smaller the unit cell gets, and may affect the resulting microstructures as well as the predicted mechanical behavior. In computational practice, self-intersecting fibers only occur rarely, that is, for individual fibers. Therefore, its influence on the effective stiffness seems to be limited. However, excluding self-intersection is vital for finding a non-intersecting configuration, that is, without proper means, the algorithm would not converge on a regular basis.

4.4 | On the Realized Fiber Curvatures and Their Effect on the Mechanical Properties

In this section, we compare the realized fiber curvature of the microstructures generated with the fSAM algorithm with or without the introduced fiber curvature control. Additionally, we aim to study the influence of the fiber curvature on the effective properties. Therefore, we first generate ten microstructures without the fiber curvature control. We consider the setup described in Section 4.2 with the cubic cell dimensions $Q_i = 400\mu$m, which is sufficient for representativity, see Section 4.3. The individual runtimes to generate the ten microstructures as well as the realized volume-weighted DSCs $\overline{K}^r$ are plotted in Figure 9, represented by the blue dots. We observe a mean runtime of about 16 s. Furthermore, the realized volume-weighted DSCs $\overline{K}^r$ are in a close range with a small mean value of 0.084. Thus, the fibers are rather straight.

In addition, we aim to compare the results with the novel formulation of the fSAM algorithm, including the fiber curvature control. Therefore, we consider the volume-weighted DSCs in the set

$$\overline{K} \in \{0.06, 0.084, 0.1, 0.15, 0.2, 0.25\} \tag{4.3}$$

where we also account for the mean volume-weighted DSC of the microstructures generated without fiber curvature control. Microstructures generated with three different volume-weighted DSCs are shown in Figure 6. For each value in Equation (4.3), we generate ten realizations and plot the runtime in Figure 9. We observe that the runtime has a convex shape with a minimum at $\overline{K} = 0.1$, where the mean runtime is 9.7 s. For the lower bound of the volume-weighted DSC $\overline{K} = 0.06$, the mean runtime is 42.6 s and for the upper bound of the volume-weighted DSC $\overline{K} = 0.25$, the mean runtime is even higher with 81.7 s. Still, all microstructures are generated in less than two minutes. Let us compare the runtime at $\overline{K} = 0.084$ with the runtime of the microstructure generation without curvature control. Then, we observe that the runtimes are within the same range, which underlines that the additional term in the objective function retains the efficiency of the algorithm.

We aim to discuss the reasons for the higher runtimes for very low and extremely high DSCs. Generating microstructures with low fiber curvature is more demanding, especially due to two reasons. First, microstructure generation for long fiber reinforced composites with straight fibers is known to be a difficult task in general due to the inflexibility of the fibers to fill small spaces. The second reason concerns the opposing algorithmic fiber movement induced by minimizing the non-overlap condition and the DSC constraint, which disturbs the convergence behavior of the fSAM algorithm. To be more precise, the non-overlap condition leads to a change in fiber geometry towards more bent fibers, as they are easier to pack without fiber-overlap, whereas the DSC constraint aims to straighten the fibers. The increase in runtime for higher DSCs is mainly caused by the local curvature constraint, which is violated more often when a higher DSC is desired, increasing the complexity of the root finding.

The plot in Figure 9 shows another advantage of the extension for a fiber curvature control. Whereas the realizable degrees of curvature are extremely limited when generating microstructures without curvature control, the novel formulation is capable of generating microstructures with volume-weighted DSCs in a wide range. Thus, it is possible to study the influence of the fiber curvature on the effective elastic behavior, and we visualize the computed Young's moduli in Figure 9b. First, we notice that the realizations without curvature control are close to the results for the microstructure generation with fiber curvature control. Furthermore, the results reveal a significant influence of the fiber curvature on the Young's moduli. To be more precise, the Young's moduli are decreasing with increasing fiber curvature, and the highest relative difference is observed for the Young's modulus E_1. Whereas the Young's modulus E_1 is 8.53 GPa on average for the volume-weighted DSC $\overline{K} = 0.06$, the modulus drops to 7.65 GPa for the volume-weighted DSC $\overline{K} = 0.25$, which is a relative decrease of 10.31%. Also, the Young's moduli E_2 and E_3 reveal a relative decrease of 8.46% and 5.02% between the smallest and the highest fiber curvature. At first glance, it may appear counterintuitive that increasing the curvature decreases the stiffness in the transversal directions as well. When one imagines a straight fiber becoming curved, this seems to increase the number of fibers in the transversal directions, which should lead to an increase in stiffness in those directions. However, because our microstructure generation algorithm controls the fiber orientation tensor separately from the curvature, it compensates for those effects by also re-orienting segments of other fibers, thereby increasing curvature without increasing the number of fibers in the transversal directions. Therefore, the only effect on the transversal stiffness is due to the fibers in all directions being more bent, that is, less stiff to loading along the fiber direction. Thus, the effective properties in all directions are significantly lower if the fiber curvature is more emphasized, and the study reveals that the influence of the fiber curvature needs to be considered when generating representative volume elements for long fiber reinforced composites. Comparing the results to the influence of other microstructural descriptors of fiber-reinforced composites, the stiffness appears to be more sensitive to the fiber curvature than to the mean fiber length in case of long fibers [33, 36], but less sensitive than to the fiber orientation distribution or the fiber volume fraction [54].

4.5 | Study on the Maximum Segment Length for Varying Degrees of Curvature

We investigate the influence of the maximum segment length on both the runtime of the microstructure generation and the effective elastic properties of the microstructures. According to a previous study [41], considering rather small fiber curvature, the maximum segment length has a significant influence on the runtime but a negligible influence on the effective properties. In this section, we aim to investigate whether this conclusion may also be drawn for varying degrees of curvature.

Therefore, we extend the study from Section 4.4 and consider the maximum segment lengths

$$\overline{\ell} \in \{15\mu\text{m}, 20\mu\text{m}, 25\mu\text{m}, 30\mu\text{m}, 35\mu\text{m}, 40\mu\text{m}\} \tag{4.4}$$

The runtime for ten generated microstructures is plotted in Figure 10. We consider the configurations with the volume-weighted DSC $\overline{K} \in [0.15, 0.25]$ first. For this range, we observe a monotonic increase in the mean runtime for all maximum segment lengths. For example, for the maximum segment length $\overline{\ell} = 15\mu$m, we observe an increase in the mean runtime from 150.8 s to 1047.4 s. Thus, the generation of microstructures with a higher degree of curvature turns out to be more challenging. Additionally, the mean runtime is smaller for larger maximum segment lengths, that is, when fewer segments are considered. For the maximum segment length $\overline{\ell} = 40\mu$m and the volume-weighted DSC $\overline{K} = 0.25$, the mean runtime is only 16.3s, which 64 times smaller than for the maximum segment length $\overline{\ell} = 15\mu$m. Due to the smaller segment number, less collision checks are necessary. Additionally, the movement of the fibers in each optimization step is computationally less expensive for a coarser segmentation of the fibers [41].

For the lower range of the volume-weighted DSC $\overline{K} \in [0.06, 0.15]$, we still observe a monotonic increase for the smallest maximum segment length $\overline{\ell} = 15\mu$m. However, the highest maximum segment length $\overline{\ell} = 40\mu$m shows a monotonic decrease. Fibers with small segments offer high flexibility to use empty spaces even for small degrees of curvature. In contrast, it is

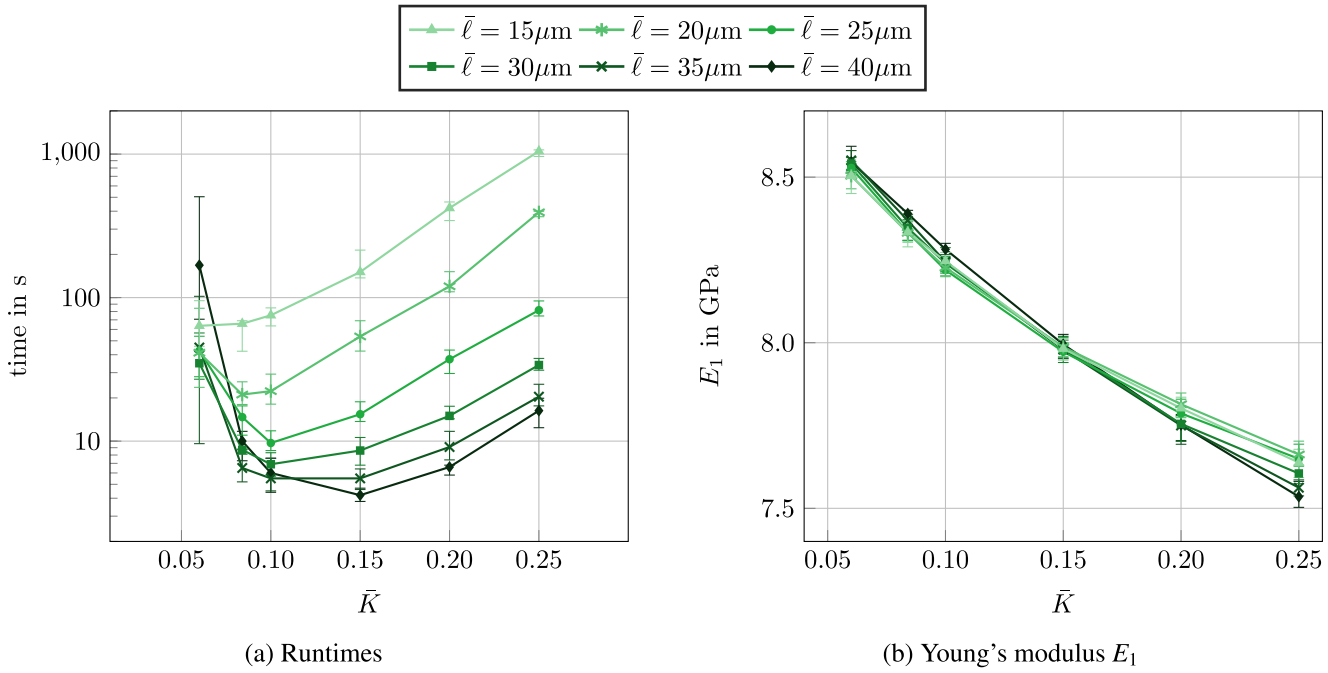

(a) Runtimes

(b) Young's modulus E_1

FIGURE 10 | Comparison of the runtimes for the microstructure generation (a) and the Young's moduli (b) in terms of different maximum segment lengths $\overline{\ell}$.

quite challenging to pack microstructures with the considered combination of the fiber volume fraction, the fiber lengths, and the fiber orientation distribution with large maximum segment lengths and small degrees of curvature. Considering the smallest volume-weighted DSC $\overline{K} = 0.06$, it turns out that the mean runtime for the maximum segment length $\overline{\ell} = 40\mu$m is even higher than for the maximum segment length $\overline{\ell} = 15\mu$m. With decreasing maximum segment lengths, we observe that the mean runtimes fall below the runtime for the maximum segment length $\overline{\ell} = 15\mu$m as more flexibility is induced.

Besides the effect on the runtimes of the microstructure generator, we aim to study the influence of the maximum segment lengths on the effective elastic properties. Therefore, we report on the Young's modulus E_1 in Figure 10b. For the lower range of the volume-weighted DSC $\overline{K} \in [0.06, 0.20]$, we observe a close match below 1% relative difference for all maximum segment lengths. For the upper bound of the volume-weighted DSC $\overline{K} = 0.25$, the results reveal a slightly larger deviation, which is still below 1.5%. Due to the elevated degree of fiber curvature, higher angles between adjacent segments are formed, especially for larger maximum segment lengths. These increased angles may induce stress peaks during the computational homogenization and thus may lead to a reduction of the effective Young's modulus. Hence, it is emphasized that, for higher curvature values, the chosen maximum segment length (which acts as a discretization parameter) must be carefully considered. If the segment length is too large, it may lead to a distortion of the results, making it critical to ensure that the segment length is small enough to avoid these stress-induced reductions in elasticity.

Let us connect the discussion on the influence of the maximum segment length to the approximation of the local curvature for a polygonal chain, see Equation (2.24). As the segment length serves as the stepsize of the finite differences formulation, the accuracy of the local curvature approximation significantly depends on the selected segment length. In case of small segment lengths, the curvature approximation is rather reliable, because the directional changes are well captured. However, for large segment lengths, the approximation does not reflect the actual local geometry anymore: The local discontinuities in the direction are averaged over longer distances, leading to a significant underestimation of the local curvature. Especially for pronounced curvature, this effect leads to a loss of geometrical detail as the sharp angles between adjacent segments are smoothed out. Transferred to the curvature constraint (3.8), the local curvature approximation leads to an increase of the admissible angles between adjacent segments for increasing segment lengths. Eventually, in case of too large segment lengths, the actual local curvature is not constrained to such a degree that stress peaks at the junction between two segments are prevented. Thus, the aforementioned stress peaks for high DSCs may be induced.

5 | Summary and Conclusion

This work presents an algorithm for generating curvature-controlled microstructures of long fiber reinforced composites. As this algorithm allows the control of average fiber curvature as a separate parameter from the usually considered fiber volume fraction, aspect ratio, and orientation distribution, it allows to investigate the relationship between curvature and composite properties.

The algorithm is based on the fused Sequential Addition and Migration (fSAM) algorithm for fiber-reinforced composite generation. Accordingly, we model the fibers as polygonal chains consisting of spherocylinder segments, which are parametrized

by relative orientations, such that they always remain connected, with only the starting point of the chain being an absolute position. As this parameter space is a curved manifold, we describe how gradient calculations for the optimization process take into account the manifold's metric. Adding to this optimization algorithm, we extended the objective function by the volume-weighted deviation from straight curve (DSC), which we compute as the trace of the local second-order fiber orientation tensor's covariance for each single fiber, and then averaging. This particular choice of average curvature parameter leads to gradually curved fibers without zig-zagging or sharp bends. In addition, we found that specifying the DSC imposes a lower bound on the average local curvature, such that increasing the DSC increases the curvature of the microstructure. With the novel DSC measure and its implementation within the framework of the fSAM algorithm, we significantly improve the curvature control methods integrated in microstructure generation tools compared to previous algorithms, for example, the SAM algorithms for long fibers [33] or the fSAM algorithm [41], which only constrain the maximum angle between adjacent segments, or the microstructure generation tool introduced by Fliegener et al. [36], which includes no curvature control at all.

We applied the algorithm to an example material consisting of a polypropylene matrix reinforced with glass fibers to study the realizability of extreme values of the curvature parameter and its influence on the stiffness of the composite. To briefly summarize:

- For the strongly textured fiber orientation distribution considered, the non-curvature-controlled fSAM algorithm tends towards a small curvature, with a mean of the realized volume-weighted DSCs $\overline{K}^{r} = 0.084$ and a low variance. By comparison, DSCs from 0.064 to 0.25 are realizable with the new algorithm.
- The new algorithm has comparable runtimes to the non-curvature-controlled fSAM at similar curvature values. Both high and low curvature microstructures are computationally expensive to realize, with mean runtimes up to eight times longer than for medium-curvature microstructures.
- Resolution studies show that for both high and low average curvatures, the resolution-induced stiffness error is of the same order of magnitude, meaning that high-curvature microstructures do not appear to require particularly fine resolutions.
- The magnitude of the representativity error appears to be similar at both extremes of fiber curvature. We found periodic microstructures containing roughly 340 fibers to be within 1% representativity error, that is, microstructures generated by our algorithm do not need to be particularly large to deliver accurate results.
- The segment length, a numerical parameter arising from the discretized fiber description, appears to have a negligible effect on the effective mechanical properties for low curvatures, as for the non-curvature-controlled fSAM algorithm. For higher curvatures, large segment lengths lead to underestimation of the stiffness, which we explain by sharp angles between adjacent segments, which lead to stress concentration in the adjacent material. The segment length's effect on the runtime is considerable, with longer segments leading to order-of-magnitude quicker calculations except for very low curvature values. Careful consideration of the segment length is therefore necessary when dealing with strongly curved fibers.
- Finally, we quantified the effect of the curvature on the stiffness, showing a monotonically decreasing stiffness with increasing curvature. This effect was most pronounced for the Young's modulus in the preferred fiber alignment direction, which showed a difference between both extremes of about 10%. With the stiffness being this sensitive to curvature, we consider curvature control an important aspect of fiber-reinforced microstructure generation.

To summarize, we extended the fSAM algorithm by adding curvature control. This does not noticeably increase the numerical expense, yet allows for control over an important microstructural parameter, the average fiber curvature, which can significantly affect the elastic properties of fiber composites.

Author Contributions

Celine Lauff: Conceptualization, Methodology, Software, Validation, Formal analysis, Investigation, Data curation, Writing – original draft, Writing – review and editing, Visualization, Project administration. **Maximilian Krause:** Methodology, Formal analysis, Writing – original draft, Writing – review and editing. **Matti Schneider:** Conceptualization, Resources, Writing – review and editing, Supervision, Project administration, Funding acquisition. **Thomas Böhlke:** Resources, Writing – review and editing, Supervision, Project administration, Funding acquisition. All authors read and approved the manuscript.

Acknowledgments

We thank the anonymous reviewers for their valuable comments and suggestions, which improved the manuscript. The partial support by the German Research Foundation (DFG) within the International Research Training Group "Integrated engineering of continuous-discontinuous long fiber reinforced polymer structures" (GRK 2078)—project number 255730231—is gratefully acknowledged. Maximilian Krause and Matti Schneider gratefully acknowledge the support from the European Research Council within the Horizon Europe program—project 101040238. Open Access funding enabled and organized by Projekt DEAL.

Conflicts of Interest

The authors declare no conflicts of interest.

Data Availability Statement

The data that support the findings of this study are available from the corresponding author upon reasonable request.

References

1. J. Görthofer, N. Meyer, T. D. Pallicity, et al., "Virtual Process Chain of Sheet Molding Compound: Development, Validation and Perspectives," *Composites Part B: Engineering* 169 (2019): 133–147.

2. H. Schüle and P. Eyerer, *Polymer Engineering 2*, 2nd ed. (Springer-Vieweg Verlag, 2020).

3. N. Meyer, S. Gajek, J. Görthofer, et al., "A Probabilistic Virtual Process Chain to Quantify Process-Induced Uncertainties in Sheet Molding Compounds," *Composites Part B: Engineering* 249 (2023): 110380.

4. R. F. de Paiva, M. Bisiaux, J. Lynch, and E. Rosenberg, "High Resolution x-Ray Tomography in an Electron Microprobe," *Review of Scientific Instruments* 67, no. 6 (1996): 2251–2256.

5. H. Shen, S. Nutt, and D. Hull, "Direct Observation and Measurement of Fiber Architecture in Short Fiber-Polymer Composite Foam Through Micro-CT Imaging," *Composites Science and Technology* 64, no. 13–14 (2004): 2113–2120.

6. F. Buck, B. Brylka, V. Müller, et al., "Two-Scale Structural Mechanical Modeling of Long Fiber Reinforced Thermoplastics," *Composites Science and Technology* 117 (2015): 159–167.

7. C. Kuhn, I. Walter, O. Taeger, and T. Osswald, "Experimental and Numerical Analysis of Fiber Matrix Separation During Compression Molding of Long Fiber Reinforced Thermoplastics," *Journal of Composites Science* 1, no. 1 (2017): 2.

8. J. Blarr, T. Sabiston, C. Krauß, et al., "Implementation and Comparison of Algebraic and Machine Learning Based Tensor Interpolation Methods Applied to Fiber Orientation Tensor Fields Obtained From CT Images," *Computational Materials Science* 228 (2023): 112286.

9. K. Matouš, M. G. D. Geers, V. G. Kouznetsova, and A. Gillman, "A Review of Predictive Nonlinear Theories for Multiscale Modeling of Heterogeneous Materials," *Journal of Computational Physics* 330 (2017): 192–220.

10. J. Fish, G. J. Wagner, and S. Keten, "Mesoscopic and Multiscale Modelling in Materials," *Nature Materials* 20, no. 6 (2021): 774–786.

11. A. Elmasry, W. Azoti, S. A. El-Safty, and A. Elmarakbi, "A Comparative Review of Multiscale Models for Effective Properties of Nano- and Micro-Composites," *Progress in Materials Science* 132 (2023): 101022.

12. S. M. Kozlov, "Averaging of Differential Operators With Almost Periodic Rapidly Oscillating Coefficients," *Mathematics of the USSR-Sbornik* 35, no. 4 (1979): 481–498.

13. G. C. Papanicolaou and S. R. S. Varadhan, "Boundary Value Problems With Rapidly Oscillating Random Coefficients," in *Random Fields, Vol. I, II (Esztergom, 1979), Volume 27 of Colloq. Math. Soc. János Bolyai* (North-Holland Publishing Company, 1981), 835–873.

14. T. Kanit, S. Forest, I. Galliet, V. Mounoury, and D. Jeulin, "Determination of the Size of the Representative Volume Element for Random Composites: Statistical and Numerical Approach," *International Journal of Solids and Structures* 40, no. 13–14 (2003): 3647–3679.

15. K. Sab and B. Nedjar, "Periodization of Random Media and Representative Volume Element Size for Linear Composites," *Comptes Rendus. Mécanique* 333, no. 2 (2005): 187–195.

16. M. Schneider, M. Josien, and F. Otto, "Representative Volume Elements for Matrix-Inclusion Composites - a Computational Study on the Effects of an Improper Treatment of Particles Intersecting the Boundary and the Benefits of Periodizing the Ensemble," *Journal of the Mechanics and Physics of Solids* 158 (2022): 104652.

17. S. Bargmann, B. Klusemann, J. Markmann, et al., "Generation of 3D Representative Volume Elements for Heterogeneous Materials: A Review," *Progress in Materials Science* 96 (2018): 322–384.

18. D. Jeulin, *Morphological Models of Random Structures*, vol. 53 (Springer International Publishing, 2021).

19. B. Widom, "Random Sequential Addition of Hard Spheres to a Volume," *Journal of Chemical Physics* 44, no. 10 (1966): 3888–3894.

20. J. Feder, "Random Sequential Adsorption," *Journal of Theoretical Biology* 87, no. 2 (1980): 237–254.

21. L. Chen, B. Gu, J. Zhou, and J. Tao, "Study of the Effectiveness of the RVEs for Random Short Fiber Reinforced Elastomer Composites," *Fibers and Polymers* 20, no. 7 (2019): 1467–1479.

22. W. Tian, X. Chao, M. W. Fu, and L. Qi, "An Advanced Method for Efficiently Generating Composite RVEs With Specified Particle Orientation," *Composites Science and Technology* 205 (2021): 108647.

23. Z. Li, Z. Liu, Y. Xue, and P. Zhu, "A Novel Algorithm for Significantly Increasing the Fiber Volume Fraction in the Reconstruction Model With Large Fiber Aspect Ratio," *Journal of Industrial Textiles* 51, no. 1 (2022): 506–530.

24. A. Bahmani, R. Y. Nooraie, T. L. Willett, and J. Montesano, "A Sequential Mobile Packing Algorithm for Micromechanical Assessment of Heterogeneous Materials," *Composites Science and Technology* 237 (2023): 110008.

25. C. Lauff, M. Schneider, J. Montesano, and T. Böhlke, "An Orientation Corrected Shaking Method for the Microstructure Generation of Short Fiber-Reinforced Composites With Almost Planar Fiber Orientation," *Composite Structures* 322 (2023): 117352.

26. D. Coelho, J.-F. Thovert, and P. M. Adler, "Geometrical and Transport Properties of Random Packings of Spheres and Aspherical Particles," *Physical Review E* 55, no. 2 (1997): 1959–1978.

27. Y. Pan, L. Iorga, and A. A. Pelegri, "Numerical Generation of a Random Chopped Fiber Composite RVE and Its Elastic Properties," *Composites Science and Technology* 68, no. 13 (2008): 2792–2798.

28. S. R. Williams and A. P. Philipse, "Random Packings of Spheres and Spherocylinders Simulated by Mechanical Contraction," *Physical Review E* 67, no. 5 (2003): 051301.

29. M. Schneider, "Convergence of FFT-Based Homogenization for Strongly Heterogeneous Media," *Mathematical Methods in the Applied Sciences* 38, no. 13 (2015): 2761–2778.

30. A. Mehta and M. Schneider, "A Sequential Addition and Migration Method for Generating Microstructures of Short Fibers With Prescribed Length Distribution," *Computational Mechanics* 70, no. 4 (2022): 829–851.

31. A. Mehta and M. Schneider, "A Maximum-Entropy Length-Orientation Closure for Short-Fiber Reinforced Composites," *Computational Mechanics* 74, no. 3 (2024): 615–640.

32. B. Drach, D. Kuksenko, and I. Sevostianov, "Effect of a Curved Fiber on the Overall Material Stiffness," *International Journal of Solids and Structures* 100 (2016): 211–222.

33. M. Schneider, "An Algorithm for Generating Microstructures of Fiber-Reinforced Composites With Long Fibers," *International Journal for Numerical Methods in Engineering* 123, no. 24 (2022): 6197–6219.

34. T. Dai, Y. Wei, C. Tao, and J. Huang, "Mechanical Model of Stiffness Coefficients Prediction of Curved Fiber Reinforced Composites Considering Fiber Distribution and Aggregation," *Composite Structures* 321 (2023): 117277.

35. Q. C. P. Bourgogne, "Influence of Fibre Curvature and Orientation on the Mechanical Properties of Injected Irregular Short Hemp Fibres Reinforced Polypropylene," *Journal of Thermoplastic Composite Materials* 37, no. 9 (2024): 2963–2986.

36. S. Fliegener, M. Luke, and P. Gumbsch, "3D Microstructure Modeling of Long Fiber Reinforced Thermoplastics," *Composites Science and Technology* 104 (2014): 136–145.

37. A. I. Abd El-Rahman and C. L. Tucker, "Mechanics of Random Discontinuous Long-Fiber Thermoplastics. Part II: Direct Simulation of Uniaxial Compression," *Journal of Rheology* 57, no. 5 (2013): 1463–1489.

38. S. G. Advani and C. L. Tucker, III, "A Numerical Simulation of Short Fiber Orientation in Compression Molding," *Polymer Composites* 11, no. 3 (1990): 164–173.

39. D. Dray, P. Gilormini, and G. Régnier, "Comparison of Several Closure Approximations for Evaluating the Thermoelastic Properties of an Injection Molded Short-Fiber Composite," *Composites Science and Technology* 67, no. 7–8 (2007): 1601–1610.

40. A. Bernasconi, F. Cosmi, and P. J. Hine, "Analysis of Fibre Orientation Distribution in Short Fibre Reinforced Polymers: A Comparison Between Optical and Tomographic Methods," *Composites Science and Technology* 72, no. 16 (2012): 2002–2008.

41. C. Lauff, M. Schneider, J. Montesano, and T. Böhlke, "Generating Microstructures of Long Fiber Reinforced Composites by the Fused Sequential Addition and Migration Method," *International Journal for Numerical Methods in Engineering* 125, no. 22 (2024): e7573.

42. C. Lauff, M. Schneider, and T. Böhlke, "Microstructure Generation of Long Fiber Reinforced Hybrid Composites Using the Fused Sequential Addition and Migration Method," *Journal of Thermoplastic Composite Materials* (2025): 1–39.

43. T. Böhlke, F. Henning, A. Hrymak, L. Kärger, K. A. Weidenmann, and J. T. Wood, *Continuous–Discontinuous Fiber-Reinforced Polymers: An Integrated Engineering Approach* (Carl Hanser Verlag, 2019).

44. R. S. Bay and C. L. Tucker, III, "Fiber Orientation in Simple Injection Moldings. Part II: Experimental Results," *Polymer Composites* 13, no. 4 (1992): 332–341.

45. P. A. Hessman, T. A. Riedel, F. Welschinger, K. Hornberger, and T. Böhlke, "Microstructural Analysis of Short Glass Fiber Reinforced Thermoplastics Based on x-Ray Micro-Computed Tomography," *Composites Science and Technology* 183 (2019): 107752.

46. K. Breuer, A. Spickenheuer, and M. Stommel, "Statistical Analysis of Mechanical Stressing in Short Fiber Reinforced Composites by Means of Statistical and Representative Volume Elements," *Fibers* 9, no. 5 (2021): 32.

47. A. W. Goodman and G. Goodman, "Generalizations of the Theorems of Pappus," *American Mathematical Monthly* 76, no. 4 (1969): 355–366.

48. K.-I. Kanatani, "Distribution of Directional Data and Fabric Tensors," *International Journal of Engineering Science* 22, no. 2 (1984): 149–164.

49. S. G. Advani and C. L. Tucker, III, "The Use of Tensors to Describe and Predict Fiber Orientation in Short Fiber Composites," *Journal of Rheology* 31, no. 8 (1987): 751–784.

50. J. S. Cintra and C. L. Tucker, III, "Orthotropic Closure Approximations for Flow-Induced Fiber Orientation," *Journal of Rheology* 39, no. 6 (1995): 1095–1122.

51. J. K. Bauer and T. Böhlke, "Variety of Fiber Orientation Tensors," *Mathematics and Mechanics of Solids* 27, no. 7 (2022): 1185–1211.

52. U. Pinkall and O. Gross, *Differential Geometry: From Elastic Curves to Willmore Surfaces*. Compact Textbooks in Mathematics Series (Springer International Publishing, 2024).

53. P. V. Araújo, *Differential Geometry* (Springer Nature, 2024).

54. M. Schneider, "The Sequential Addition and Migration Method to Generate Representative Volume Elements for the Homogenization of Short Fiber Reinforced Plastics," *Computational Mechanics* 59, no. 2 (2017): 247–263.

55. M. Krause, J. M. Hausherr, B. Burgeth, C. Herrmann, and W. Krenkel, "Determination of the Fibre Orientation in Composites Using the Structure Tensor and Local X-Ray Transform," *Journal of Materials Science* 45, no. 4 (2010): 888–896.

56. O. Wirjadi, K. Schladitz, P. Easwaran, and J. Ohser, "Estimating Fibre Direction Distributions of Reinforced Composites From Tomographic Images," *Image Analysis & Stereology* 35, no. 3 (2016): 167–179.

57. P. Pinter, S. Dietrich, B. Bertram, L. Kehrer, P. Elsner, and K. A. Weidenmann, "Comparison and Error Estimation of 3D Fibre Orientation Analysis of Computed Tomography Image Data for Fibre Reinforced Composites," *NDT & E International* 95 (2018): 26–35.

58. P. Kennedy and R. Zheng, *Flow Analysis of Injection Molds*, 2nd ed. (Carl Hanser Verlag, 2013).

59. N. Meyer, L. Schöttl, L. Bretz, A. N. Hrymak, and L. Kärger, "Direct Bundle Simulation Approach for the Compression Molding Process of Sheet Molding Compound," *Composites Part A: Applied Science and Manufacturing* 132 (2020): 105809.

60. V. Müller and T. Böhlke, "Prediction of Effective Elastic Properties of Fiber Reinforced Composites Using Fiber Orientation Tensors," *Composites Science and Technology* 130 (2016): 36–45.

61. J. K. Bauer and T. Böhlke, "On the Dependence of Orientation Averaging Mean Field Homogenization on Planar Fourth-Order Fiber Orientation Tensors," *Mechanics of Materials* 170 (2022): 104307.

62. K. Breuer, M. Stommel, and W. Korte, "Analysis and Evaluation of Fiber Orientation Reconstruction Methods," *Journal of Composites Science* 3, no. 3 (2019): 67.

63. S. K. Kugler, A. Kech, C. Cruz, and T. Osswald, "Fiber Orientation Predictions—A Review of Existing Models," *Journal of Composites Science* 4, no. 2 (2020): 69.

64. T. Karl, D. Gatti, B. Frohnapfel, and T. Böhlke, "Asymptotic Fiber Orientation States of the Quadratically Closed Folgar–Tucker Equation and a Subsequent Closure Improvement," *Journal of Rheology* 65, no. 5 (2021): 999–1022.

65. T. Karl, M. Schneider, and T. Böhlke, "On Fully Symmetric Implicit Closure Approximations for Fiber Orientation Tensors," *Journal of Non-Newtonian Fluid Mechanics* 318 (2023): 105049.

66. S. Montgomery-Smith, W. He, D. A. Jack, and D. E. Smith, "Exact Tensor Closures for the Three-Dimensional Jeffery's Equation," *Journal of Fluid Mechanics* 680 (2011): 321–335.

67. S. Montgomery-Smith, D. A. Jack, and D. E. Smith, "The Fast Exact Closure for Jeffery's Equation With Diffusion," *Journal of Non-Newtonian Fluid Mechanics* 166, no. 7–8 (2011): 343–353.

68. C. V. Chaubal and L. G. Leal, "A Closure Approximation for Liquid-Crystalline Polymer Models Based on Parametric Density Estimation," *Journal of Rheology* 42, no. 1 (1998): 177–201.

69. A. G. García, *Random Packings via Mechanical Contraction* (Universiteit Utrecht, 2015).

70. P. Petersen, *Riemannian Geometry, 171 of Graduate Texts in Mathematics* (Springer International Publishing, 2016).

71. DOW Chemical Company, "C711–70RNA Polypropylene Resin," *Product Information* (2003).

72. PPG Fiber Glass, "TufRov 4575. Data Sheet," (2013).

73. F. Garesci and S. Fliegener, "Young's Modulus Prediction of Long Fiber Reinforced Thermoplastics," *Composites Science and Technology* 85 (2013): 142–147.

74. H. Moulinec and P. Suquet, "A Fast Numerical Method for Computing the Linear and Nonlinear Mechanical Properties of Composites," *Comptes Rendus de L'académie Des Sciences. Série II* 318, no. 11 (1994): 1417–1423.

75. H. Moulinec and P. Suquet, "A Numerical Method for Computing the Overall Response of Nonlinear Composites With Complex Microstructure," *Computer Methods in Applied Mechanics and Engineering* 157, no. 1–2 (1998): 69–94.

76. M. Schneider, F. Ospald, and M. Kabel, "Computational Homogenization of Elasticity on a Staggered Grid," *International Journal for Numerical Methods in Engineering* 105, no. 9 (2016): 693–720.

77. J. Zeman, J. Vondřejc, J. Novák, and I. Marek, "Accelerating a FFT-Based Solver for Numerical Homogenization of Periodic Media by Conjugate Gradients," *Journal of Computational Physics* 229, no. 21 (2010): 8065–8071.

78. S. Brisard and L. Dormieux, "Combining Galerkin Approximation Techniques With the Principle of Hashin and Shtrikman to Derive a New FFT-Based Numerical Method for the Homogenization of Composites,"

Computer Methods in Applied Mechanics and Engineering 217-220 (2012): 197–212.

79. M. Schneider, "A Dynamical View of Nonlinear Conjugate Gradient Methods With Applications to FFT-Based Computational Micromechanics," *Computational Mechanics* 66, no. 1 (2020): 239–257.

80. M. Schneider, "A Review of Nonlinear FFT-Based Computational Homogenization Methods," *Acta Mechanica* 232, no. 6 (2021): 2051–2100.

81. S. C. Cowin, "The Relationship Between the Elasticity Tensor and the Fabric Tensor," *Mechanics of Materials* 4, no. 2 (1985): 137–147.

82. J. Görthofer, M. Schneider, F. Ospald, A. Hrymak, and T. Böhlke, "Computational Homogenization of Sheet Molding Compound Composites Based on High Fidelity Representative Volume Elements," *Computational Materials Science* 174 (2020): 109456.

83. R. Hill, "Elastic Properties of Reinforced Solids: Some Theoretical Principles," *Journal of the Mechanics and Physics of Solids* 11, no. 5 (1963): 357–372.

84. W. J. Drugan and J. R. Willis, "A Micromechanics-Based Nonlocal Constitutive Equation and Estimates of Representative Volume Element Size for Elastic Composites," *Journal of the Mechanics and Physics of Solids* 44, no. 4 (1996): 497–524.

85. A. Gloria and F. Otto, "An Optimal Variance Estimate in Stochastic Homogenization of Discrete Elliptic Equations," *Annals of Probability* 39, no. 3 (2011): 779–856.

86. P. Betsch, "The Discrete Null Space Method for the Energy Consistent Integration of Constrained Mechanical Systems: Part I: Holonomic Constraints," *Computer Methods in Applied Mechanics and Engineering* 194, no. 50–52 (2005): 5159–5190.

87. J. Angeles and S. Lee, "The Modelling of Holonomic Mechanical Systems Using a Natural Orthogonal Complement," *Transactions of the Canadian Society for Mechanical Engineering* 13, no. 4 (1989): 81–89.

Appendix A

Properties of the DSC

A Simple Representation Formula for the DSC

We demonstrate the formula (2.17)

$$K_f = 1 - \|\boldsymbol{A}_f\|^2 \tag{A1}$$

to hold. We modify Equation (2.13) to obtain

$$\begin{aligned} K_f &= \frac{1}{L}\int_0^L \|\boldsymbol{A}_f\|^2 - 2\,\boldsymbol{A}_f \cdot \big(\boldsymbol{c}'(s)\otimes\boldsymbol{c}'(s)\big) + \|\boldsymbol{c}'(s)\otimes\boldsymbol{c}'(s)\|^2 \; ds \\ &= \frac{1}{L}\left(L\|\boldsymbol{A}_f\|^2 - 2\,\boldsymbol{A}_f \cdot \underbrace{\int_0^L \boldsymbol{c}'(s)\otimes\boldsymbol{c}'(s)\; ds}_{L\,\boldsymbol{A}_f} + \underbrace{\int_0^L \underbrace{\|\boldsymbol{c}'(s)\otimes\boldsymbol{c}'(s)\|^2}_{1}\; ds}_{L} \right) \\ &= \|\boldsymbol{A}_f\|^2 - 2\,\|\boldsymbol{A}_f\|^2 + 1 \\ &= 1 - \|\boldsymbol{A}_f\|^2 \end{aligned} \tag{A2}$$

Upper and Lower Bounds of the DSC

The purpose of this section is to establish the bounds (2.14)

$$0 \le K_f \le \frac{2}{3} \tag{A3}$$

for the DSC. The lower bound is a direct consequence of the definition (2.13). For the upper bound, we use the representation (2.17)

$$K_f = 1 - \|\boldsymbol{A}_f\|^2 \tag{A4}$$

We insert the fiber orientation tensor of second order in diagonal form (2.6), and find that the DSC may be computed with two of the three eigenvalues, for example,

$$K_f = 1 - \left(a_1^2 + a_2^2 + a_3^2\right) = 1 - \left(a_1^2 + a_2^2 + \left(1 - a_1 - a_2\right)^2\right) \tag{A5}$$

The possible values attained by the DSC are determined by the fiber orientation triangle, as shown in Figure 3. It turns out that the DSC takes values in the range

$$0 \le K_f \le \frac{2}{3} \tag{A6}$$

where the parameter is zero only if the fiber is straight and has the value 2/3 only if the orientation state of the fiber is isotropic.

Vanishing DSC Implies a Straight Fiber

We would like to establish the validity of the characterization (2.15)

$$K_f = 0 \quad \text{if and only if} \quad \boldsymbol{c}''(s) = \boldsymbol{0} \quad \text{for all} \quad s \in [0, L] \tag{A7}$$

As vanishing curvature implies that the fiber is straight, and hence the vanishing of the DSC, we restrict to showing the converse statement.

So let us assume that the DSC K_f vanishes. By definition (2.13) and due to the assumed continuity of the second derivative $\boldsymbol{c}''$, the pointwise equation

$$\boldsymbol{A}_f = \boldsymbol{c}'(s)\otimes\boldsymbol{c}'(s) \quad \text{holds for all} \quad s \in [0, L] \tag{A8}$$

As the left-hand side does not depend on the arc length parameter s, differentiating the latter equation yields

$$\boldsymbol{0} = \boldsymbol{c}''(s)\otimes\boldsymbol{c}'(s) + \boldsymbol{c}'(s)\otimes\boldsymbol{c}''(s) \quad \text{for all} \quad s \in [0, L] \tag{A9}$$

Computing the linear map of the vector $\boldsymbol{c}'(s)$ by the Equation (A9) yields

$$\boldsymbol{0} = \underbrace{\boldsymbol{c}'(s)\cdot\boldsymbol{c}'(s)}_{=1}\,\boldsymbol{c}''(s) + \underbrace{\boldsymbol{c}'(s)\cdot\boldsymbol{c}''(s)}_{=0}\,\boldsymbol{c}'(s) \equiv \boldsymbol{c}''(s) \quad \text{for all} \quad s \in [0, L] \tag{A10}$$

where we used the arc length condition (2.2) which implies that the vectors $\boldsymbol{c}''(s)$ and $\boldsymbol{c}'(s)$ are orthogonal. In particular, the curvature (2.9) vanishes, which was to be shown.

Lower Bound for the Average Curvature

We intend to justify that the estimate (2.16)

$$K_f \le 2\big(L\,\overline{\kappa}_f\big)^2 \tag{A11}$$

holds. The latter is a direct consequence of the following Poincaré-Wirtinger inequality

$$\int_0^L \|\boldsymbol{T}(s) - \overline{\boldsymbol{T}}\|^2 \; ds \le L\left(\int_0^L \|\boldsymbol{T}'(s)\| \; ds\right)^2 \tag{A12}$$

valid for a continuously differentiable tensor-valued function $\boldsymbol{T}$ on the interval $[0, L]$ and where we denote by

$$\overline{\boldsymbol{T}} = \frac{1}{L}\int_0^L \boldsymbol{T}(s) \; ds \tag{A13}$$

the averaged tensor.

Assuming the validity of the inequality (A12) for the moment, we apply this estimate to the tensor field

$$\boldsymbol{T}(s) = \boldsymbol{c}'(s) \otimes \boldsymbol{c}'(s), \quad s \in [0, L] \tag{A14}$$

corresponding to a parametrized fiber (2.1). We notice

$$\overline{\boldsymbol{T}} = \boldsymbol{A}_f \tag{A15}$$

$$\int_0^L \|\boldsymbol{T}(s) - \overline{\boldsymbol{T}}\|^2 \; ds = L \; K_f \tag{A16}$$

$$\boldsymbol{T}'(s) = \boldsymbol{c}''(s) \otimes \boldsymbol{c}'(s) + \boldsymbol{c}'(s) \otimes \boldsymbol{c}''(s), \quad s \in [0, L] \tag{A17}$$

To proceed, we compute the Frobenius norm of the derivative $\boldsymbol{T}'(s)$ explicitly, and obtain

$$\|\boldsymbol{T}'(s)\|^2 = 2(\|\boldsymbol{c}'(s)\|^2\|\boldsymbol{c}''(s)\|^2 + (\boldsymbol{c}'(s) \cdot \boldsymbol{c}''(s))^2) \equiv 2 \; \|\boldsymbol{c}''(s)\|^2 \tag{A18}$$

where we used the normalization condition (2.2) of a curve parametrized by arc length and the subsequent orthogonality of the vectors $\boldsymbol{c}'(s)$ and $\boldsymbol{c}''(s)$. In particular, we might express the integral on the right-hand side of the inequality (A12) in the form

$$\int_0^L \|\boldsymbol{T}'(s)\| \; ds = \sqrt{2} \int_0^L \|\boldsymbol{c}''(s)\| \; ds = L \; \sqrt{2} \; \overline{\kappa}_f \tag{A19}$$

Collecting these observations, the inequality (A12) becomes

$$K_f \leq 2\big(L \; \overline{\kappa}_f\big)^2 \tag{A20}$$

that is, the desired estimate (A11).

Thus, it remains to establish the validity of the Poincaré-Wirtinger inequality (A12)

$$\int_0^L \|\boldsymbol{T}(s) - \overline{\boldsymbol{T}}\|^2 \; ds \leq L \bigg(\int_0^L \|\boldsymbol{T}'(s)\| \; ds \bigg)^2 \tag{A21}$$

which is a bit non-standard due to the L^2-norm on the left-hand side and the $W^{1,1}$-norm on the right-hand side.

First, we re-write the term $\boldsymbol{T}(s) - \overline{\boldsymbol{T}}$ as an integral

$$\boldsymbol{T}(s) - \overline{\boldsymbol{T}} = \boldsymbol{T}(s) - \frac{1}{L} \int_0^L \boldsymbol{T}(y) \; dy = \frac{1}{L} \int_0^L [\boldsymbol{T}(s) - \boldsymbol{T}(y)] \; dy \tag{A22}$$

In particular, the triangle inequality for integrals implies the estimate

$$\|\boldsymbol{T}(s) - \overline{\boldsymbol{T}}\| \leq \frac{1}{L} \int_0^L \|\boldsymbol{T}(s) - \boldsymbol{T}(y)\| \; dy \tag{A23}$$

We use the fundamental theorem of calculus to express the difference $\boldsymbol{T}(s) - \boldsymbol{T}(y)$ in the form

$$\boldsymbol{T}(s) - \boldsymbol{T}(y) = \int_y^s \frac{d}{dz}[\boldsymbol{T}(z)] \; dz = \int_y^s \boldsymbol{T}'(z) \; dz \tag{A24}$$

which implies the estimate

$$\|\boldsymbol{T}(s) - \boldsymbol{T}(y)\| \leq \int_y^s \big\|\boldsymbol{T}'(z)\big\| \; dz \leq \int_0^L \big\|\boldsymbol{T}'(z)\big\| \; dz = \|\boldsymbol{T}'\|_{L^1} \tag{A25}$$

Inserting this finding into the inequality (A23) yields the bound

$$\|\boldsymbol{T}(s) - \overline{\boldsymbol{T}}\| \leq \|\boldsymbol{T}'\|_{L^1} \quad s \in [0, L] \tag{A26}$$

Squaring and integrating yields the bound

$$\|\boldsymbol{T} - \overline{\boldsymbol{T}}\|_{L^2}^2 = \int_0^L \|\boldsymbol{T}(s) - \overline{\boldsymbol{T}}\|^2 \; ds \leq L \; \|\boldsymbol{T}'\|_{L^1}^2 \tag{A27}$$

that is, the desired inequality (A12) holds.

Appendix B

Adapted Gradient Descent Approach on the Curved Manifold

The goal of this appendix is to give background information on the equations governing the geodesics of the considered polygonal chain, and to derive the adapted gradient descent approach with respect to the curved manifold (3.23).

The equations governing the geodesics are derived from the principle of minimizing the kinetic energy functional on the manifold. This approach may be interpreted as a constrained mechanical system, where no external forces are acting on the system, and the motion is solely driven by the system's intrinsic kinetic energy [86, 87]. For the considered polygonal chain defined on the manifold $\mathcal{R}_i$ (2.22), the equations governing the geodesics may be expressed in the form of a d'Alembert type constrained mechanical system [41]

$$\begin{aligned} \mathbf{P}(\mathbf{q}_i)^{\mathrm{T}} \; \mathbf{G}_i \; \ddot{\mathbf{q}}_i &= \mathbf{0}, \\ \boldsymbol{\Phi}_1(\mathbf{q}_i) &= \mathbf{0} \end{aligned} \tag{B1}$$

including the null space matrix

$$\mathbf{P}(\mathbf{q}_i) = \begin{bmatrix} \mathbf{1}_{3\times3} & \mathbf{0}_{3\times3} & \cdots & \mathbf{0}_{3\times3} \\ \mathbf{0}_{3\times2} & \mathbf{P}^1(\mathbf{p}_i^1) & \cdots & \mathbf{0}_{3\times2} \\ \vdots & \vdots & \ddots & \vdots \\ \mathbf{0}_{3\times2} & \mathbf{0}_{3\times2} & \cdots & \mathbf{P}^n(\mathbf{p}_i^n) \end{bmatrix} \quad \text{with} \quad \mathbf{P}^a(\mathbf{p}_i^a) = \Big[\mathbf{r}^a(\mathbf{p}^a) \;\; \mathbf{s}^a(\mathbf{p}^a)\Big] \tag{B2}$$

with the column vectors of the submatrices $\mathbf{P}^a(\mathbf{p}_i^a)$

$$\begin{aligned} &\mathbf{r}^a(\mathbf{p}_i^a) = \mathbf{R}^a(\mathbf{p}_i^a) \; \mathbf{e}_1, \quad \mathbf{s}^a(\mathbf{p}_i^a) = \mathbf{R}^a(\mathbf{p}_i^a) \; \mathbf{e}_2 \\ &\text{with} \quad \mathbf{R}^a(\mathbf{p}_i^a) = \big(\mathbf{e}_3 \cdot \mathbf{p}_i^a\big)\mathbf{1}_{3\times3} + \big(\mathbf{e}_3 \times \mathbf{p}_i^a\big)\times + \frac{\big(\mathbf{e}_3 \times \mathbf{p}_i^a\big) \otimes \big(\mathbf{e}_3 \times \mathbf{p}_i^a\big)}{1 + \mathbf{e}_3 \cdot \mathbf{p}_i^a} \end{aligned} \tag{B3}$$

and the constant symmetric positive-definite metric matrix $\mathbf{G}$

$$\mathbf{G}_i = \begin{bmatrix} n_i \; \hat{\mathbf{Q}}^2 & f_1 \; \ell_i \; \hat{\mathbf{Q}} & f_2 \; \ell_i \; \hat{\mathbf{Q}} & \cdots & f_n \; \ell_i \; \hat{\mathbf{Q}} \\ & f_{d,1} \; \mathbf{1}_{3\times3} & f_2 \; \ell_i^2 \; \mathbf{1}_{3\times3} & \cdots & f_n \; \ell_i^2 \; \mathbf{1}_{3\times3} \\ & & \ddots & & \vdots \\ & & & \ddots & f_n \; \ell_i^2 \; \mathbf{1}_{3\times3} \\ \text{sym} & & & & f_{d,n} \; \mathbf{1}_{3\times3} \end{bmatrix}$$

$$\text{with} \quad f_a = n_i - a + \frac{1}{2} \quad \text{and}$$

$$f_{d,a} = \varepsilon\big(\ell_i, D\big) + \ell_i^2\Big(n_i - a + \frac{1}{4}\Big) \tag{B4}$$

With the equations governing the geodesics (B1), we proceed to compute the exponential map taking a given point $\mathbf{q} \in \mathcal{R}_i$ on the manifold as well as a tangent vector $\mathbf{v} \in T_{\mathbf{q}}\mathcal{R}_i$ and moving along the unique geodesic with starting point $\mathbf{q}$ and starting direction $\mathbf{v}$. An efficient numerical approach to integrate the d'Alembert type constrained mechanical system to obtain the exponential mapping is discussed in Lauff et al. [41]. Using the exponential mapping, the iterates of the optimization problem read

$$\mathbf{q}_i^{k+1} = \exp_{\mathbf{q}_i^k}\Big(-\tau \; \nabla_{\mathbf{q}_i} F\big(\mathbf{f}_1^k, \ldots, \mathbf{f}_N^k\big)\Big), \quad k = 0, 1, \ldots \tag{B5}$$

where τ denotes the stepsize, $\nabla_{\mathbf{q}_i} F\big(\mathbf{f}_1^k, \ldots, \mathbf{f}_N^k\big)$ stands for the gradient of the objective function with respect to the coordinate vector $\mathbf{q}_i$ and $\exp_{\mathbf{q}}(\mathbf{v})$ refers to the exponential mapping.